CO₂ and CO temporal variability over Mexico City from ground-based total column and surface measurements

Noémie Taquet[1], Wolfgang Stremme[1], María Eugenia González del Castillo[1], Victor Almanza[1], Alejandro Bezanilla[1], Olivier Laurent[2], Carlos Alberti[3], Frank Hase[3], Michel Ramonet[2], Thomas Lauvaux[4], Ke Che[4], Michel Grutter[1]

[1]Instituto de Ciencias de la Atmósfera y Cambio Climático, Universidad Nacional Autónoma de México, México
[2]Laboratoire des Sciences du Climat et de l'Environnement (LSCE), IPSL, CEA-CNRS-UVSQ, Université Paris-Saclay, Gif-sur-Yvette, France
[3]Institute of Meteorology and Climate Research (IMK-ASF), Karlsruhe Institute of Technology (KIT), Karlsruhe, Germany
[4]Groupe de Spectrométrie Moléculaire et Atmosphérique (GSMA), Université de Reims-Champagne Ardenne, UMR CNRS 7331, Reims, France

Correspondence to: Noémie Taquet (noemi.taquet@gmail.com)

Abstract. Precise estimates of greenhouse gas (GHG) emissions and sinks are critical for understanding the carbon cycle and identifying key factors in the human-induced climate change feedback. Recent efforts were focused on reconciling bottom-up and top-down GHG emissions estimates, in particular on the city scale, using both space-based and ground-based atmospheric composition measurements that still show serious discrepancies. In this study, we explore the variability of the CO and CO_2 emissions from the Mexico City Metropolitan Area (MCMA) from long-term time-resolved total column measurements using solar absorption Fourier Transform Infrared Spectroscopy (FTIR). Measurements were performed at three stations, two of them located in the urban area at two opposite sides of Mexico City center and the third in a mountainous background site. Using a simple model and the mixed layer height from a ceilometer, the GHG concentration in the mixed layer and the CO/CO_2 ratio were determined from the total column observations and compared to surface measurements using Cavity ring-down spectroscopy (CRDS). Finally, combining the ground-based total column and space-based TROPOMI CO measurements, we estimate the annual CO and CO_2 MCMA emissions based on a simple model, i.e.: without recourse to complex transport models. By this way, we study the inter-annual variability of the CO and CO_2 MCMA anthropogenic emissions, and relate it to the main natural or anthropogenic changes occurring during the last decade, such as the 2015-2016 El Niño period or the COVID-19 lock-down event.

1 Introduction

The greenhouse gas (GHG) mitigation strategies implemented in megacities following the 1997 Kyoto Protocol and the 2015 Paris Agreement play a crucial role in the global action plan to mitigate climate change, given that cities are accountable for more than 70% of the global anthropogenic emissions (Duren and Miller, 2012). With the recent progress in space-based and ground-based remote GHG measurements in terms of accuracy, spatial coverage/resolution and temporal frequency, GHG emissions can increasingly be constrained by comparing bottom-up and top-down estimates. Top-down approaches are generally based on ground or space-based atmospheric measurements coupled with inverse modelling, using 3D-Eulerian (i.e: WRF-Chem) or Lagrangian and hybrid (i.e: STILT, Hysplit) approaches (Wu et al., 2018, Che et al., 2022; Lian et al., 2023). The quantification of anthropogenic CO_2 enhancements from cities using satellite data e.g: GOSAT (Wang et al., 2019), OCO-2 (Ye

45   et al., 2020) or TanSat (Liu et al., 2018) is still challenging due to the sparsity of the observations, the low signal

46   from the anthropogenic contribution compared to the background levels and biogenic contribution, and some

47   inconveniences inherent to space-measurements such as the non-negligible aerosol effects (Wang et al., 2020 and

48   references therein). Some studies have estimated the urban enhancements of anthropogenic CO_2 concentrations

49   along with CO and NO_2 from satellite measurements, as these air pollutants can serve as tracers of anthropogenic

50   CO_2 (Silva et al.,2013; Park et al., 2021 and references therein). The CO/CO_2 ratio is often used to determine the

51   combustion efficiency of the cities (Park et al., 2021 and references therein). With the development of a new

52   generation of space-based observatories, such as Sentinel-5P and OCO-2,3, the evolution of GHGs at the city scale

53   can now be characterised with a finer temporal and spatial resolution (Kiel et al., 2021) but more validation efforts

54   are needed. As inverse modelling is likely undermined by the approximations used for defining the emission

55   patterns, transport processes and meteorology, top-down approaches may lead to discrepancies in emissions

56   estimates, in particular in sites with complex orography.

57   Ground-based total column FTIR instruments provide valuable long-time concentration measurements of

58   GHG and pollutant reactive species, as well as anthropogenic tracers, constituting a key element to validate

59   regional and local inventories. Some studies reported estimates of CO_2 and CH_4 emissions from large urban areas

60   (Babenhauserheide et al., 2018 in Tokyo; Hedelius et al., 2018 in the California Southern Coast Air Basin

61   California megacity), using data from high-resolution FTIR instruments (i.e: Bruker IFS120/5HR) contributing to

62   the Total Column Carbon Observing Network (TCCON). Nevertheless, only a few TCCON stations are located in

63   urban areas (Toon et al., 2009; Chevallier et al., 2011; Sussman et al., 2020). The development of the COllaborative

64   Carbon Column Observing Network (COCCON, Frey et al., 2019), using a new generation of portable low spectral

65   resolution FTIR spectrometers (EM27/SUN, Gisi et al., 2012; Hase et al., 2016) able to simultaneously measure

66   the CO_2, CO, H_2O and CH_4 average total columns with a similar quality as TCCON, has considerably densified

67   the number of measurements in urban environments. Some studies reported emission estimates for big cities by

68   means of the deployment of several EM27/SUN instruments at strategic sites throughout the cities (Hase et al.,

69   2015 and Zhao et. al., 2019 in Berlin; Vogel et al., 2019 in Paris; Makarova et al., 2021 in St Petersbourg; Zhou et

70   al., 2022 in Beijing and Xianghe; Che et al. 2022, in Beijing; Rißmann et al., 2022 for Munich) coupling

71   measurements with inverse modelling. Most of these studies were based on short-term campaign observations,

72   applying the Differential Column Methodology (DCM, Chen et al., 2016) or dedicated dispersion models (Hase

73   et al., 2016), coupled with simple mass balance-based methods or inverse modelling to derive emissions. Most of

74   these studies reported significant discrepancies between the estimates, depending on the models used (Viatte et

75   al., 2017).

76   In this study, we aimed to determine the Mexico City Metropolitan Area (MCMA) CO_2 and CO emissions

77   using ground-based FTIR and surface measurements, without resorting to complex dispersion and/or chemistry

78   transport models. The MCMA, with a population around 22 million inhabitants, is in the top ten most populous

79   cities in the world and ranks among the major emitters of GHGs in North America. The available information of

80   GHGs emission estimates are mainly based on the inventories reported by the Ministry of the Environment of

81   Mexico City (SEDEMA), which is updated every two years, but lagging several years behind. In the report based

82   on 2018, the latest published before the COVID19-lock-down (2020), a total emission of 75.2 Mt CO2-eq is

83   estimated for the MCMA, 87% of which is attributed to fossil fuel combustion and 58% originates from the

84   transport sector (SEDEMA Inventory, 2018). The Mexico City government is actively engaged in the C40 Climate

85   Change Program and implemented significant policy measures since 2008, including promoting sustainable

86   transportation systems, implementing energy efficiency measures, increasing the use of renewable energy sources,

87   and adopting green building practices. On a national scale, the country is committed to reduce its GHGs emissions

88   by 35% by 2030 with respect to its base level, as stated in the last Nationally Determined Contributions report

89   (NDC-2022, UNFCCC). To assess the effect of the national and local mitigation policies, the installation of

90   ground-based GHG measurement networks and the refinement of bottom-up estimates by comparing them with

91   the top-down method (i.e: inverse modelling) is of critical importance to obtain a comprehensive GHGs database

92   that can serve as follow-up of the mitigation actions.

93   The Institute of Atmospheric Sciences and Climate Change (ICAyCC, Spanish acronym) at UNAM

94   (Universidad Nacional Autónoma de México) deployed in the last decade a wide range of surface gas sensors and

95   ground-based remote sensing instruments across the MCMA (Grutter, et al., 2003; Molina et al., 2010; Bezanilla

96   et al., 2014; Stremme et al., 2009; 2013; Baylon et al., 2017) in the frame of research projects related to air quality

97   assessment and validation of ground-based satellite products. Since 2013, UNAM has contributed to the Network

98   for the Detection of Atmospheric Composition Change (NDACC), performing continuous composition

99   measurements of the free troposphere from the high altitude Altzomoni Atmospheric Observatory (ALTZ) station,

100   located 60 km southeast of Mexico City at 3985 m a.s.l. Baylon et al., (2017) reported the background CO_2

101   variability and trend from this station between 2013 and 2016. Stremme et al., (2013) reported the first top-down

102   estimate of carbon monoxide (CO) emissions for the MCMA, based on FTIR CO total column measurements and

103   the Infrared Atmospheric Sounding Interferometer (IASI) data. These authors derived the CO_2 emissions for the

104   MCMA using the CO emission estimates and the average CO/CO_2 ratio reported in Grutter (2003), using FTIR

105   measurements. In 2018, the Mexican/French "Mexico City's Regional Carbon Impacts (MERCI-CO2)" project

106   (coordinated by UNAM and LSCE) was launched aiming to assess the CO_2 emissions from MCMA using

107   EM27/SUN measurements and inverse modelling to evaluate the effectiveness of the mitigation strategies

108   implemented by the local authorities. Xu et al., (submitted) examined the performance of a modelling system based

109   on WRF-Chem to assess the whole-city emissions using the EM27/SUN measurements deployed in the frame of

110   the MERCI-CO2 project. The complex orography of the region posed a challenge in the atmospheric transport

111   simulations and thus for the top-down estimates using inverse modelling. Indeed, Mexico City is situated in a high

112   altitude basin (~2300 m. a.s.l.), surrounded by mountains reaching up to 5.6 km a.s.l., and is prone to accumulate

113   anthropogenic emissions, especially during the dry season, when the atmospheric boundary layer ventilation is

114   limited (Burgos-Cuevas et al., 2023). The boundary layer dynamics in the basin and the wind surface circulation

115   is complex, due to the temperature contrasts and rough topography.

116   In this study, we report the long-term (2013-2021) variability of the CO_2 and CO total columns and

117   surface concentrations (from 2014) above the MCMA using long-term ground-based FTIR and surface Cavity

118   Ring-Down Spectroscopic (CRDS) measurements. Using the mixed layer height data from the continuous

119   ceilometer measurements at UNAM, we examined the consistency of the surface and total column measurements

120   of our network. We also determined an average CO/CO_2 ratio based on FTIR and surface measurements at different

121   temporal resolutions (from daily to intraday). Then, using the spatial distribution of TROPOMI CO column

122   measurements, we explore the potential of our FTIR network to capture the variability of the megacity CO and

123   CO_2 emissions using a simplified model, i.e.: without recourse to complex numerical simulations. Our estimates

124   are compared with the available bottom-up and previous top-down estimates.

125   **2 Sites, instrumentation and measurement protocols**

126   We used in this study the column-averaged dry-air mole fractions of CO_2 and CO (XCO$_2$ and XCO) from

127   three permanent FTIR stations distributed in a radius of 100 km around MCMA (Fig. 1), and the surface

128   measurements performed at UNA and ALTZ sites. The measurement periods for the different instruments at each

129   site are reported in Table 1. The VAL station is located at the northern part of the city in a highly industrialised

130   zone. The UNA station is situated at the south of the city in the main campus of UNAM. The third station is the

131   ALTZ background site (3985 m a.s.l.), located 60 km ESE from UNAM, within the Izta-Popo National Park. The

132   equipment of the different stations and measurement protocols are described in the following sub-sections.
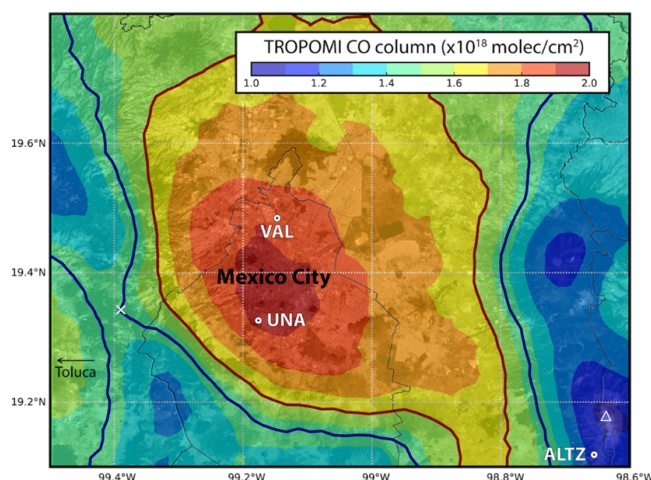
133

134 **Figure 1: Map of the ALTZ, UNA and VAL stations and average distribution (2018-2022) of carbon monoxide total**
135 **columns over the Mexico City Metropolitan Area (MCMA) calculated from the TROPOMI CO product. The average**
136 **total column can be decomposed into two main contributors: i) a background of around 1.45×10^{18} molec.cm^{-2} (limits**
137 **represented by blue contour lines) and ii) the local influence corresponding to the carbon monoxide emitted on the same**
138 **day. The total columns are highly influenced by the topography which is clearly visible over the highest terrains of the**
139 **region, near the Volcanoes Popocatepétl and Iztaccíhuatl (close to the ALTZ station) at the south east of Mexico City.**
140 **The mountains of Ajusco are located southwest of Mexico City. The enhancement in the center of the metropolitan area**
141 **reflects the carbon monoxide locally emitted on the same day.**

142

143

144   *Table1: Instrumentation and measurement periods used in this study.*

Station	Instrument	Measurement period	Product
ALTZ	IFS120/5HR	01/01/2013 - 01/06/2021	XCO and XCO$_2$
	EM27/SUN #038	21/10/2020 - 20/12/2020 & 10/02/2021 - 22/02/2021	XCO and XCO$_2$
	EM27/SUN #104	07/02/2020 - 18/02/2020	XCO and XCO$_2$
	CRDS G2401 Picarro	15/11/2015 - 01/06/2021	Surface CO and CO$_2$

UNA	Vertex	15/11/2015 - 20/06/2017	XCO
	EM27/SUN #038	07/05/2021 - 25/05/2021	XCO and XCO_2
	EM27/SUN #062	17/03/2016 - 01/06/2017	XCO_2
		01/06/2017 - 01/06/2021	XCO and XCO_2
	EM27/SUN #104	04/04/2019 - 19/09/2019	XCO and XCO_2
	CDRS G2401 Picarro	15/11/2015 - 01/06/2021	Surface CO and CO_2
	CL31 Vaisala ceilometer	15/11/2015 - 01/06/2021	Mixed Layer Height
VAL	EM27/SUN #104	23/09/2019 - 01/06/2021	XCO and XCO_2

145

2.1 The UNA station: Total columns, surface concentrations and mixed-layer height measurements

146

147   Atmospheric total columns of several gas species, such as O_3, NH_3, CH_4, CO, and HCHO have

148 continuously been measured at UNA since 2010 (Bezanilla et al., 2014; Plaza-medina et al., 2017; Baylon et al.,

149 2017; Rivera-Cardenas et al., 2021; Herrera et al., 2022) using solar absorption FTIR spectroscopy.

150 Measurements are performed in the mid-infrared (MIR) and near-infrared (NIR) spectral ranges using a Bruker

151 model Vertex 80 spectrometer. The instrument has a Maximum optical Path Difference (MPD) of 12 cm

152 (corresponding to a spectral resolution of 0.075 cm^{-1}) and is equipped with two detectors, a liquid-nitrogen cooled

153 mercury-cadmium-telluride (MCT) and InGaAs detectors. Solar absorption measurements are performed using a

154 home-built solar tracker. A full description of the instrumental set-up and measurement protocols is given in

155 Bezanilla et al. (2014) and Plaza-Medina et al. (2017). The CO measurements are routinely performed in the MIR

156 spectral range with a spectral resolution of 0.1 cm^{-1}, using the MCT detector.

157   In March 2016, an EM27/SUN spectrometer was implemented at UNA to continuously measure XCO_2,

158 XCH_4, XH_2O, XCO total columns from solar NIR spectra with a spectral-resolution of 0.5 cm^{-1} (MPD of 1.8 cm).

159 The spectrometer is equipped with its own solar tracker (Bruker CAMTracker; Gisi et al., 2011) capturing and

160 redirecting the solar beam into a RockSolid^{TM} pendulum interferometer equipped with a Quartz beamsplitter. The

161 EM27/SUN, with serial number #62 installed at the UNA station (hereafter EM27-SUN_62), was initially operated

162 with a standard InGaAs-diode detector sensitive to the 5500-11000 cm^{-1} spectral range, to which a second InGaAs

163 detector with Ge filter was added in 2017 for CO measurements through a second channel (4000 – 5500 cm^{-1})

164 (Hase et al., 2016). Further details on the technical characteristics and systematic performance evaluation of the

165 EM27/SUN spectrometer are given in Frey et al., (2019) and Alberti et al., (2022). The spectrometer was installed

166 in a home-made protective box, including a remotely-controlled dome cover, a GPS and a PCE-THB-40 data-

167 logger for precise timing and surface pressure measurements. Double sided forward-backward interferograms are

168 routinely recorded with a scanner velocity of 10 kHz, so that the recording time of one measurement (averaging

169 10 IFGs scans) is close to one minute.

170   Additionally, CO_2, CO, CH_4 and H_2O surface measurements are continuously performed at the UNA

171 station using a Cavity Ring-Down Spectrometer (CRDS, model G2401 from Picarro Inc.). The CRDS spectrometer

172 uses a laser to quantify the spectral features of gas-phase molecules in an optical cavity offering effectively of up

173 to 20 km absorption path length. Frequency shifts are prevented with a high-precision-wavelength monitor and

174 temperature and pressure are precisely controlled by the analyzer. The quantification is improved by the

175 simultaneous spectral analysis of the measured gases. A calibration system using 3 gas standards provided by the

176 National Oceanic and Atmospheric Administration Earth System Research Laboratory (NOAA ESRL), traceable

177   to the WMO2007 scale, was set up in 2018 at UNA and in 2019 at ALTZ. Data collected before the installation of

178   the calibration systems were corrected with calibration coefficients obtained in 2018. The sampling inlet using

179   Synflex tubing was placed at 24 m a.g.l. at UNA station and includes a Nation air dryer, as described in detail by

180   González del Castillo et al. (2022). Data are continuously collected at 0.3 Hz rate and their uncertainties, calculated

181   as the standard deviation of raw data over 1-minute intervals when measuring calibration gases, are equal to 0.03

182   ppm at UNA (González del Castillo et al., 2022).

183

184   Finally, continuous mixed-layer height (MLH) measurements are performed since 2008 at UNA using a

185   CL31 ceilometer instrument (Vaisala). This is a robust commercial instrument which emits light pulses at 10 kHz

186   repeating frequency at 910 nm using an indium-gallium-arsenide diode laser. It detects the backscatters signal

187   through a single lens with a silicon avalanche photodiode. The resulting backscattering profiles have a vertical

188   resolution of 10 m and reach an altitude of 7,500 m. The profiles have been used to retrieve MLH above the city

189   since 2011 (García-Franco et al., 2018).

2.2 The ALTZ background station: Total columns and surface measurements

191   The Altzomoni Atmospheric Observatory (ALTZ) was equipped with a high-resolution FTIR

192   spectrometer (model IFS120/5HR, Bruker) in 2012, capable of measuring atmospheric spectra in the NIR and MIR

193   spectral regions with 257 cm MPD, equivalent to a spectral resolution of 0.0035 cm^{-1}. The instrument is installed

194   into a container with a motorised dome cover on the roof and a microwave communication system (60 km line-of-

195   sight to the university campus), which allows a fully-remote control of the instruments. When the dome is open, a

196   solar tracker (CAMTracker; Gisi et al., 2012) collects the solar beam and orients it toward the spectrometer

197   entrance. The spectrometer can be operated with KBr or CaF$_2$ beam splitters, 3 different detectors (MCT, InSb,

198   and InGaAs) and a set of 7 optical filters is installed in a rotating wheel. The measurement routine consists in the

199   acquisition of high (0.005 cm^{-1}), medium (0.02 cm^{-1} and 0.1 cm^{-1}) and low (0.5 cm^{-1}) resolution spectra in the NIR

200   and MIR spectral ranges using the different NDACC filters (~40 min for a complete sequence).

201   The NIR CO and CO$_2$ spectra (0.02 cm^{-1}) used in this study were recorded as the average of two scans

202   taken for approximately 38 s with a scanner speed of 40 kHz. The MIR CO spectra (0.005 cm^{-1}) are deduced from

203   the coaddition of 6 scans (<200 s) with a scanner speed of 40 kHz. Due to a spectrometer laser replacement, the

204   IFS120/5HR measurements were interrupted between November 2020 and February 2021 (Table 1). To avoid an

205   important gap in the measurements, an EM27/SUN (EM27/SUN_38) was temporarily installed at the station

206   during this period. The intercalibration factors used for combining the two types of measurements were determined

207   from previous side-by-side measurements performed during February 2021 (see Table S1 and section 3.1.3).

208   A CRDS (model G2401 from Picarro Inc.) instrument was implemented at the station in 2014 providing

209   continuous CO$_2$, CO, CH$_4$ and H$_2$O surface measurements (Gonzáles del Castillo et al., 2022). The sampling inlet

210   using Synflex tubing was placed at 4 m a.g.l. and includes a Nation air dryer (similar installation to UNA). A

211   calibration system similar to that implemented at UNA, using 3 NOAA ESRL gas standards, was set up in 2019.

212   The station also includes meteorological instruments, pressure and temperature sensors and visible cameras among

213   other instrumentation for atmospheric and environmental monitoring.

2.3 The VAL station: Total column measurements

The VAL station, located in Vallejo in the northern part of MCMA, is part of the city's air quality network (RAMA) run by SEDEMA. An EM27/SUN spectrometer (EM27/SUN_104) was installed at this station in 2019 together with a surface CO_2 sensor. The VAL spectrometer has been performing measurements with the two detectors since November 2019.

3 Data Analysis

3.1 FTIR data processing and analysis

In this study, we used the solar absorption measurements acquired by five different FTIR instruments (i.e: three EM27/SUN, a Vertex 80 and a IFS120/5HR) to estimate the XCO_2, and XCO total columns at each station. The retrieval strategies were adapted as a function of the spectral resolution and averaging kernel of each species. Table 2 summarises the different products used in this study, and their retrieval parameters.

Table 2: FTIR analysis: Description of the different FTIR products, retrieval strategies and parameters used in this study.

Instrument (spectral resolution)	Gas	Microwindows (cm^{-1})	Interfering gases	Retrieval code	Retrieval method
EM27/SUN and IFS-120/5HR LowRes (0.5 cm^{-1})	CO_2	6173.0-6390.0	H_2O, CH_4	PROFFAST	Scaling VMR COCCON strategy
	CO	4208.7-4318.8	H_2O, HDO, CH_4, HF		
	O_2	7765.0 - 8005.0	H_2O, CO_2, HF		
IFS-120/5HR (0.02 cm^{-1}) (TCCON-type)	CO_2	6180.0 – 6260.0 6310.0-6380.0	H_2O, CH_4,HDO	PROFFIT9.6	Scaling VMR
	CO	4208.7- 4257.3 4262.0 – 4318.8	CH_4, H_2O, HDO		
	O_2	7765.0-8005.0	H_2O, CO_2 , HF		
IFS-120/5HR (0.005 cm^{-1}) (NDACC-type)	CO	2057.70-2058.00 2069.56-2069.76 2157.50-2159.15	O_3, N_2O, H_2O, OCS and CO_2	PROFFIT9.6	Profile NDACC strategy
Vertex80 (0.1cm^{-1})	CO	2056.70 – 2059.00 2068.56-2069.77 2156.50-2160.15	O_3, N_2O, H_2O, OCS and CO_2	PROFFIT9.6	Profile

3.1.1 EM27/SUN spectra analysis

Double-sided interferograms from the EM27/SUN were analysed following the standardised COCCON protocol, using PREPROCESS and PROFFAST codes, developed by the KIT and made freely available (https://www.imk-asf.kit.edu/english/COCCON.php). The codes and retrieval methods are fully described in Sha et al. (2020), Frey et al. (2021) and Alberti (2023) and only briefly summarised here. The PREPROCESS algorithm generates the

233 required spectra by a Fast Fourier Transform. The processing incorporates various quality checks, as a signal
234 threshold, intensity variations during recording, requirement of proper spectral abscissa scaling, and generates
235 spectra only from raw measurements passing all checks (the remaining ones being flagged). We used the ILS
236 parameters (i.e: modulation efficiency amplitude and phase error) reported on the KIT-COCCON website
237 (https://www.imk-asf.kit.edu/english/COCCON.php) and in Alberti et al. (2022), corresponding to the initial KIT
238 calibration of the spectrometers (Frey et al., 2019, Alberti et al., 2022). The PROFFAST-PCXS module (i.e:
239 forward model of PROFFAST) pre-calculates daily lookup tables of the molecular absorption cross-sections
240 according to the meteorological parameters and gas trace VMR profiles priors. The latest PROFFAST-PCXS
241 version uses the HITRAN 2020 spectroscopic linelists (with some extensions, e.g., line mixing parameters added
242 for CH4). Here, we used the standard COCCON linelists as incorporated in the previous PROFFAST version, i.e:
243 HITRAN 2008 for CH_4, HITRAN 2012 for CO_2, a modified version of HITRAN 2009 by Toon (2014) for H_2O, a
244 TCCON standard linelist for O_2, and the same solar line list as previously used by TCCON (compiled by G.C.
245 Toon for GGG2014). The least-squares fitting code PROFFAST-INVERS retrieves the total columns by scaling
246 the prior VMR profiles iteratively until adjusting the fit to the measured spectra. The intraday variability of surface
247 pressure is considered in the retrieval, interpolated from the in-situ pressure measurements. For tying the column-
248 averaged abundances provided by COCCON to TCCON data, PROFFAST applies post-process Airmass-
249 Dependent (ADCF) and -Independent (AICF) corrections, independent from the instrument, similar as used in the
250 TCCON process (Sha et al., 2020, and Alberti, 2023). The corrections and parameters used are reported in the
251 COCCON website and Alberti, (2023).

252   We automatized and adapted the data processing to obtain a preliminary "real-time" hourly-updated
253 analysis (hereafter, AN1) for each site, additionally to the off-line treatment (hereafter, AN2) applying the standard
254 COCCON procedure. The meteorological data used in the AN1 retrieval were derived from the daily-available
255 radiosonde data, provided by Servicio Meteorologico Nacional (SMN) from measurements performed in the early
256 morning (6 AM LT) at the Mexico City International Airport. The AN1 strategy adopted fixed VMR priors for
257 each species, consisting in the averaged profile of 41 years (1980-2020) run of the Whole Atmospheric Community
258 Climate Model (WACCM), as commonly used in the NDACC community. The AN2 processing, generating the
259 COCCON standard products, used the daily TCCON meteorological data and priors (GGG2014 version of MAPs
260 files), downloaded from the Caltech server, which are based on National Centers for Environmental Prediction
261 (NCEP) reanalysis. For both AN1 and AN2 processing, we used the in situ intraday surface pressure measurements
262 from the PCE-THB-40 sensors. A correction factor was applied to the pressure measurements to take into account
263 the bias between the different pressure sensors used, previously intercompared by a few days of side-by-side
264 measurements.

265   CO_2, O_2, and CO were analysed in the 6173.0-6390.0 cm^{-1}, 7765.0- 8005.0 cm^{-1} and 4208.7- 4318.8 cm^{-1}
266 spectral windows, respectively. The XCO_2 and XCO column-averaged dry air mole fractions were calculated using
267 the O_2 retrieved total columns, according to Wunch et al. (2009):

268     $Xgas = 0.2095 \, (C_{gas} \, / \, C_{O2})$ (1)

269 where C_{gas} and C_{O2} are the target gas and O_2 total columns, respectively.
270 The real-time (AN1) and COCCON (AN2) XCO_2 and XCO products showed relative differences lower than 0.05%
271 and 5%, respectively. The results presented hereafter are based on the official COCCON products (AN2 analysis).

3.1.2 Vertex80 and IFS120/5HR spectra analysis

272

273   High (0.005 cm^{-1}) and medium (0.02 cm^{-1} and 0.1 cm^{-1}) resolution solar-absorption spectra are processed

274   using the PROFFIT9.6 code (Hase et al., 2004).

275   XCO_2 is retrieved from the NIR 0.02 cm^{-1} resolution spectra applying the procedure described in Baylon et al.

276   (2017), in which two independent CO_2 and O_2 VRM-scaling retrievals are performed using fixed WCCAM VMR

277   priors and NCEP-derived meteorological data. Spectral windows and interfering gases (Table 2) are similar to

278   those used in the standard TCCON procedure. XCO_2 is then calculated from the retrieved CO_2 and O_2 total columns

279   by applying the Eq. (1).

280   For the ALTZ analysis, CO was retrieved from the high (0.005 cm^{-1}) resolution spectra in the MIR region, applying

281   the standard NDACC procedure (Table 2). It uses a profile retrieval strategy with fixed WACCM VMR priors and

282   NCEP meteorological data. Since the O_2 specie is not analysed in the MIR region, the XCO was determined using

283   the dry air columns (C_{dryair}):

284

285
$$XCO = \frac{C_{CO}}{C_{dryair}} \qquad\qquad\qquad\qquad (2)$$

286   with:

287
$$C_{dryair} = \left(\frac{P_g}{g} \cdot m_{dryair}\right) - \left(C_{H2O}\frac{m_{H2O}}{m_{dryair}}\right) \qquad\qquad (3)$$

288

289   where C_{CO} and C_{H2O} are the retrieved CO and H_2O total columns, g the column-averaged gravity acceleration, P_g

290   the ground pressure and m_{dryair} and m_{H2O}, the dry air and H_2O molecular masses respectively. In addition, we

291   analysed XCO from the NIR spectral region to complement the MIR time-series, occasionally interrupted when

292   the liquid nitrogen was missing at the station. The CO and O_2 columns in the NIR region were analysed using

293   scaling retrievals in the same spectral windows as that used by TCCON (Table 2), but with fixed WACCM VMR

294   priors and NCEP meteorological data. XCO was calculated from the CO and O_2 retrieved total columns applying

295   the Eq. (1). To minimise the air mass dependence effect (likely low for CO), we filtered out data with a SZA >60°.

296   XCO NIR and MIR products were compared and intercalibrated (section 3.1.3).

297   For UNA, we used the XCO total columns calculated from the Vertex80 measurements to complement the

298   EM27/SUN time series during the period when it was operating with a single detector (between March 2016 and

299   September 2017). CO was analysed from the 0.1 cm^{-1} resolution spectra in the MIR spectral range, using a standard

300   NDACC profile retrieval strategy and the PROFFIT9.6 retrieval program with constant WACCM VMR priors and

301   NCEP meteorological data. Spectral windows (Table 2) were adapted following Pougatchev and Rinsland (1995).

302   Previous CO total columns time series retrieved from the same method at UNA were presented in Garcia-Franco

303   et al. (2018) and Borsdorff et al. (2018, 2020). Only the constraint of these CO retrievals were adjusted for the

304   Megacity and allowed in addition a free fitting of the mixing layer concentration, following the work by Stremme

305   et al. (2009) in which low resolution MIR- spectra with a different retrieval program have been analysed.

3.1.3 Measurement precision and FTIR product intercomparison

306

307   Side-by-side measurements were performed at the ALTZ and UNA stations on several occasions (Table1)

308   to assess the FTIR measurement precisions, to characterise the bias between the different products and to define

309 the inter-calibration factors for the XCO_2 and XCO products. We used the EM27/SUN_62 products as reference,

310 for which we previously applied the standard XCO_2 and XCO calibration factors reported in Alberti et al. (2022),

311 to inter-calibrate our results with the COCCON network and the Karlsruhe TCCON station operated by KIT. The

312 linear regression parameters from the different measurement pairs and the calibration factors are presented in the

313 Supplementary data (Table S1 and S2).

314 We found a bias lower than 0.2% and 1.0% between the three EM27/SUN, for XCO_2 and XCO respectively, and

315 a coefficient of determination (R^2) higher than 0.99.

316 On the other hand, the precision of the EM27/SUN measurements was assessed by calculating the standard

317 deviation over a 5 min-interval period, and found to be on average 2.7 ppb and 0.3 ppm for XCO and XCO_2,

318 respectively.

319 The intercomparison of the IFS120/5-HR high resolution (0.02 cm^{-1}) products and the EM27/SUN XCO_2 products

320 was performed for the daily average data used in this study. The calibration factors were determined using i) the

321 EM27/SUN XCO_2 products and ii) the IFS 120/5-HR low resolution (0.5 cm^{-1}) product (Fig. S2), processed in the

322 same way as the COCCON EM27/SUN data but having the advantage of being measured even outside the

323 campaigns carried out with the EM27/Sun. We finally found a bias around 0.4% (slope=0.996), and a coefficient

324 of determination R^2 of 0.92. This bias is in order of that expected when comparing TCCON and COCCON products

325 (Frey et al., 2019), when no empirical calibration is applied. On the other hand, a bias of 2% (and R^2=0.92) was

326 found comparing the XCO from the EM27/SUN and the Vertex (MIR) products at UNA.

327 One of the main contributions of the apparent bias observed when comparing products from different instruments

328 and using different retrieval strategies can be due to their respective Averaging Kernel (AK) which characterise

329 the smoothing error. It is especially the case in the comparison of XCO from the EM27/SUN (i.e: NIR scaling

330 retrieval product, Degree Of Freedom (DOF) =1) and from the Vertex (MIR profile-product, DOF > 2). To assess

331 this effect, we refined the comparison after smoothing the vertically resolved Vertex profiles with the EM27/SUN

332 AK (following Rodgers, 2000; Borsdorff et al., 2014, 2018) and re-calculating the smoothed Vertex total columns.

333 After this smoothing, the bias is reduced to 0.2% instead of 4.1% for the CO total columns. For the XCO product,

334 which includes the use of the surface pressure for the MIR product and the retrieved O_2 column for the NIR product

335 the bias is reduced to 0.4% instead of 3.5%.

3.2 Surface CRDS data analysis

337 The surface CO_2 and CO data acquired with the CRDS analysers were processed and averaged following

338 the procedure described in González del Castillo et al. (2022). Data were averaged and their standard deviation

339 calculated, per minute, then per hour. To extract the trend and seasonal CO and CO_2 variability, data were filtered

340 by discarding hours generally affected by transient and very local effects. Data recorded between 13 and 17h with

341 standard deviations lower than 6.0 ppm were selected for the UNA station, while nighttime data (19 to 5h) with

342 standard deviations lower than 2.0 ppm were selected for the ALTZ station, according to González del Castillo et

343 al. (2022).

3.3 Mixed Layer height from the Lidar measurements

345 The MLH is retrieved using a combined algorithm based on the gradient method and a wavelet-covariance

346 transformation as described in detail by García-Franco et al. (2018). These results were compared with radiosonde

347 data and MLH values derived from surface and vertical column densities of trace gases, and more recently Burgos-

348 Cuevas et al. (2022) used the variance of the vertical velocity from a Doppler Lidar (Wind Cube 100, Leosphere)

349 and compared with the ceilometer results at the same location. These studies show that the ceilometer retrieved

350 MLHs compare well with other techniques during the daytime (they agree within 15% with the trace gas method),

351 which are relevant for this study, whereas late afternoon and nighttime retrieved values might be affected by

352 aerosol residual layers at higher altitudes.

353 **3.4 Mixed layer CO and CO_2 concentrations from FTIR measurements**

354 Pollutant concentrations within the mixed layer are often estimated using surface measurements, although

355 surface concentrations are very sensitive to the airmass vertical transport, unlike the total columns. It is especially

356 the case within the Mexico City basin where the mixed layer has a strong diurnal dynamics controlling the vertical

357 distribution of the emitted pollutants (Stremme et al., 2009; Garcia-Franco et al., 2018). An estimate of the CO_2

358 and CO vertically averaged concentrations across the mixed layer can be made using the total columns measured

359 at the UNA and ALTZ stations. The dry air mole fraction measured at the UNA station (XCO_2^{UNA}) is the weighted

360 mean of that measured in the mixed layer (CO_2^{ML}) and in the free troposphere at the ALTZ station (XCO_2^{ALTZ}):

361

362 $$XCO_2^{UNA} = w_1 \times CO_2^{ML} + w_2 \times XCO_2^{ALTZ}$$

(4)

363 $$CO_2^{ML} = \frac{XCO_2^{UNA} - w2 \times XCO_2^{ALTZ}}{W1}$$

364

(5)

365 The weights (w1 and w2) depend on the pressure difference between the mixed-layer height (MLH) and the UNA

366 station, the pressure on top of the mixed layer is calculated assuming an exponential decay and an effective scale

367 height H_{scale} (assumed to be 8.0 km):

368

369 $$w_1 = \left(1 - e^{-\frac{MLH}{Hscale}}\right) \ and \ w_2 = \left(e^{-\frac{MLH}{Hscale}}\right)$$

(6)

370 The MLH above Mexico City was estimated using the hourly-averaged measurements of the ceilometer

371 at the UNA station. The hourly-averaged CO_2^{ML} and CO^{ML} products were calculated applying the same strategy

372 for the entire time series and are reported in Fig. 7, concurrently to the surface data.

373 **4 Results**

374 The FTIR XCO_2 and XCO daily-averaged time series and CO_2 and CO surface concentrations obtained at the

375 UNA, VAL and ALTZ stations between November 2015 and June 2021 are shown in Fig. 2. Trends and seasonal

376 variabilities were fitted using a Fourier series analysis (Eq. (7) and black and red solid lines in Fig. 2), following

377 Wunch et al. (2013):

378

379 $$f(x) = ax + \sum_{k=0}^{n} a_k \cos(2\pi kx) + b_k \sin(2\pi kx), \text{ with } n = 2$$

(7)

381   where x is the time (decimal year), a the mean growth rate (ppm/year), and a_k and b_k the Fourier coefficients

382   modulating the annual cycles. The coefficients for each gas species and station are reported in Table 3.

383

384   *Table 3: Fourier series fitting parameters for the UNA, VAL and ALTZ XCO_2 and XCO time series presented in Fig. 2, and*
385   *calculated from Eq.(7).*

Fitting parameters (ppm/year)	XCO_2, UNA Tot. Col.	XCO_2 ALTZ Tot. Col.	CO_2 UNA Surface	CO_2 ALTZ Surface	XCO UNA Tot. Col.	CO UNA Surface
a	2.25±0.02	2.40±0.01	1.6±0.1	2.48±0.02	$(-4.0±0.8)×10^{-3}$	$(-2.7±0.1)×10^{-2}$
$a1$	-1.06±0.04	-0.78±0.04	1.7±0.2	-0.39±0.05	$(-2.4±0.7)×10^{-3}$	$(6.5±0.4)×10^{-2}$
$a2$	2.11±0.04	1.93±0.04	1.1±0.2	-0.36±0.05	$(-3.2±0.8)×10^{-3}$	$(1.5±0.4)×10^{-2}$
b1	0.71±0.04	0.64±0.04	2.1±0.2	4.62±0.05	$(8.6±0.8)×10^{-3}$	$(6.5±4.0)×10^{-3}$
b2	-0.78±0.04	-0.45±0.04	-2.1±0.2	-1.69±0.05	$(-7.9±0.7)×10^{-3}$	$(-2.2±0.4)×10^{-2}$

386   **4.1 Trends and interannual variability**

387   The total column XCO_2 time series (Fig. 2A) at ALTZ and UNA show a similar mean growth rate around 2.4

388   ppm/year (2.4 and 2.3 ppm/year for ALTZ and UNA, respectively, Table 3) over the whole measurement period.

389   A similar mean growth rate is also found for the surface CO_2 time series (Table 3 and Fig. 2 B) in ALTZ (2.5

390   ppm/year). These values are consistent with those estimated at the Mauna Loa Observatory (MLO) reference

391   station for the 2016-2021 period (average of 2.5±0.5 calculated from surface data available in the NOAA site

392   https://gml.noaa.gov/ccgg/trends).

393   At the UNA station a surface mean growth rate of 1.6 ppm/year is found, lower than that observed from the total

394   column measurements. Comparing the surface mean growth rates with those reported by González del Castillo et

395   al. (2022) for the 2014-2019 period, we observe a significant difference for the UNA station (2.3 ppm/year in

396   González del Castillo et al., 2022) but very similar values for the ALTZ station (2.6 ppm/year in González del

397   Castillo et al., 2022). The difference observed at UNA could stem from (i) starting our new time series at the end

398
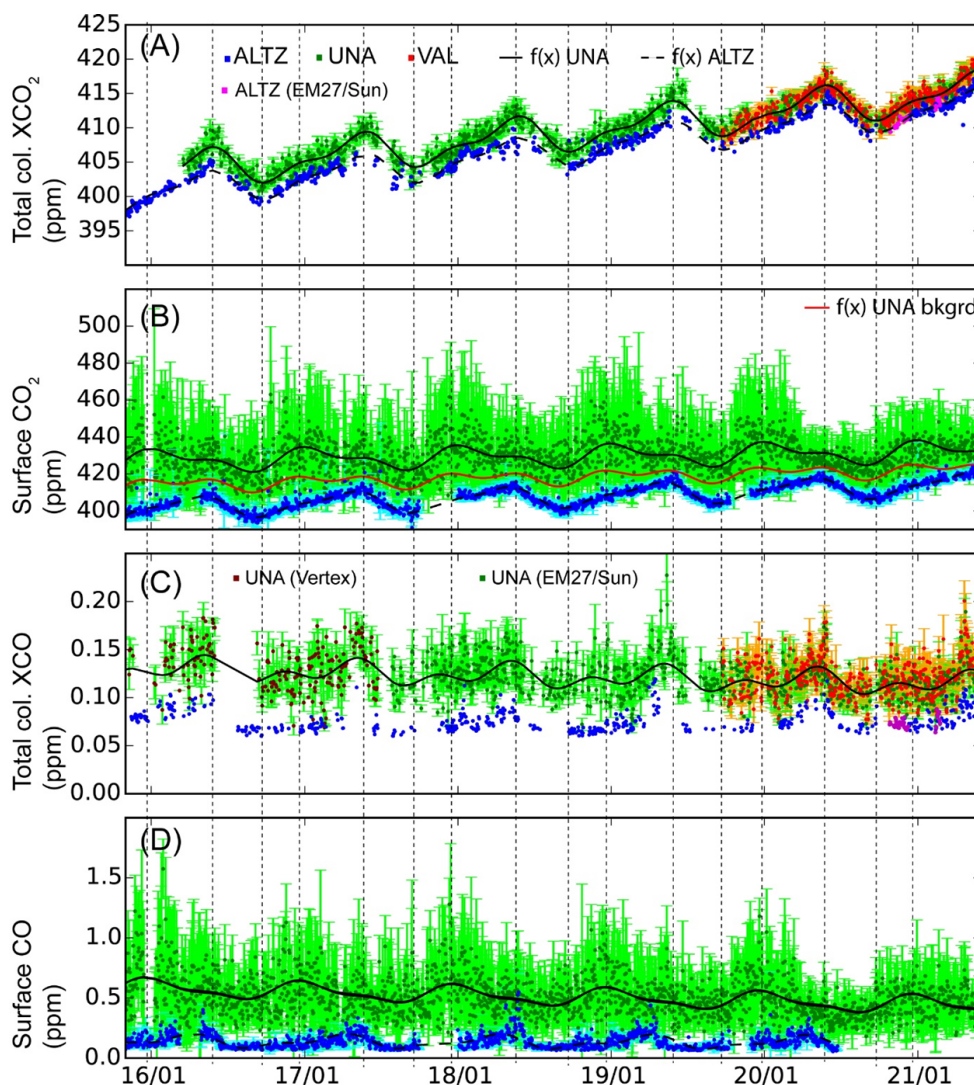
Figure 2: Time series of (A) the total column XCO₂ from the FTIR measurements (B) the CO₂ surface concentration from the CRDS measurements, (C) the total column XCO from the FTIR measurements (D) the CO surface concentration from the CRDS measurements for the UNA (in green), VAL (in red) and ALTZ (in blue) stations. For each time series, the daily average data are presented as dots with their daily standard deviations. Black traces show the annual fit calculated from the Fourier series (Eq. (7)). In (A) and (C), we distinguished between ALTZ data obtained from the IFS120/5HR (in blue) and from the EM27/Sun (in magenta) and in (C), between the CO total columns obtained from the VERTEX instrument (in brown) and the EM27/Sun (in green) at the UNA station. In (B) the red curve corresponds to the background fit, calculated following Gonzalez del Castillo et al. (2022), to determine the annual trend and seasonal cycles. Dash lines highlight the minimum and maximum of the annual cycles for the different products.

of 2015, when the annual growth rate is maximum (González del Castillo et al., 2022) and (ii) the inclusion of the

2019-2021 period, when the mean growth rate clearly decreased. At the VAL station, the total column XCO₂ time

series are found very similar to those observed at UNA stations (Fig. 2A). Figure S1 shows that 86% of the daily

average data at VAL and UNA have a difference lower than 1.0 ppm, although a large part of the comparison was

413   done during the COVID19 lock-down period (Table1), for which lower gradients are expected due to the decrease

414   of the anthropogenic emissions.

415   The interannual variability can be explored through the time series of the mean annual growth rate (AGR) and the

416   monthly-sampled annual growth rate (MAGR), according to Buchwitz et al. (2018). The MAGR is calculated by

417   month, as the difference between the monthly-average Xgas data of a year i and the monthly-averaged data of the

418   previous year ($i-1$). The AGR is obtained for each year, averaging all of the MAGR. The AGR and MAGR for

419   total column and surface measurements are presented in Fig. 4. We include data from the MLO in Fig. 4A, for

420   which the AGR (dashed black curve) was derived from the surface data available in the NOAA site.

421   At ALTZ, the interannual variability of the total column XCO_2 AGR (Fig. 4A) was found similar to that obtained

422   from both the ALTZ and MLO surface data, with a coincident peak in 2016, reaching an AGR value of 3.5 (surface

423   data) and 4.0 (total column data) ppm/year. Surface data AGR time series show a second peak in 2019, which is

424   not apparent for the total column XCO_2 time series. The time series of the MAGR (Fig. 4C) allows better

425   identifying and characterising the period and duration of the anomalies. The 2016 XCO_2 anomaly has a duration

426   up to 15 months (from October 2015 to March 2017), reaching a maximum value (around 5.0 ppm/year) between

427   March and July 2016, corresponding to a factor of 2.8 higher than the 2013-2015 base level (1.8 ppm/year).

428
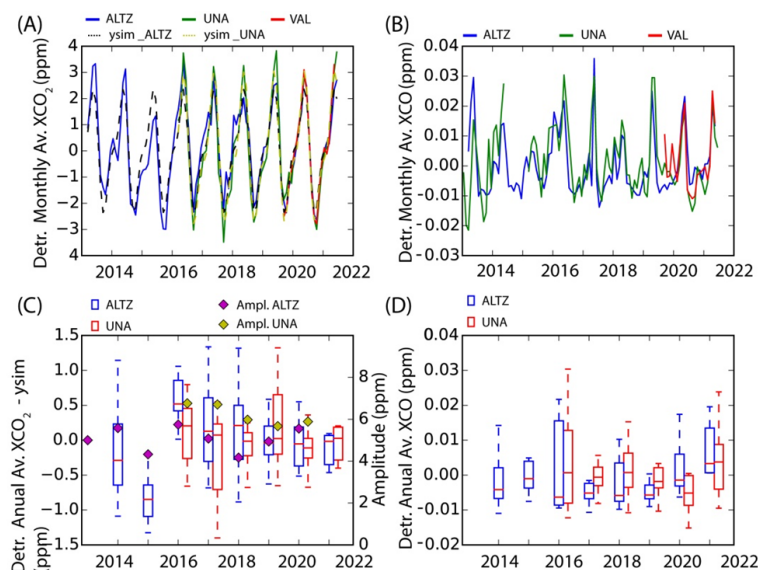
429

430   **Figure 3: Interannual and annual variability of the detrended XCO_2 and XCO total column data at the UNA, VAL and**
431   **ALTZ stations. In (C) and (D) the whisker diagrams are calculated from the monthly average detrended data. The**
432   **amplitude is determined as the max-min values.**

433

434   At UNA, the XCO_2 AGRs and MAGRs time series (Fig. 4A and C) are very similar to those observed at the ALTZ

435   station, except for the year 2020. During this year, the AGR dropped by ~20% at UNA before returning in 2021

436   to the level of the previous two years. This behaviour contrasts with the AGR observed at ALTZ, which remains

437   nearly constant between 2017 and 2021. The MAGR time series at UNA (Fig. 4C) shows that this drop is

438   dominated by the exceptionally low June and October growth rates, representing the lowest MAGR values of the

439   UNA time series. This observation is supported by the VAL MAGR, although the time series is much shorter. The

440   surface CO_2 AGR at UNA shows a much higher interannual variability, with the strongest anomaly observed in

441   2020, where the AGR is close to zero. A very clear decrease of the day-to-day and intraday CO_2 surface variability

442   is observed in Fig. 2B from April to mid-September 2020, consistent with the XCO_2 MAGR anomaly.

443
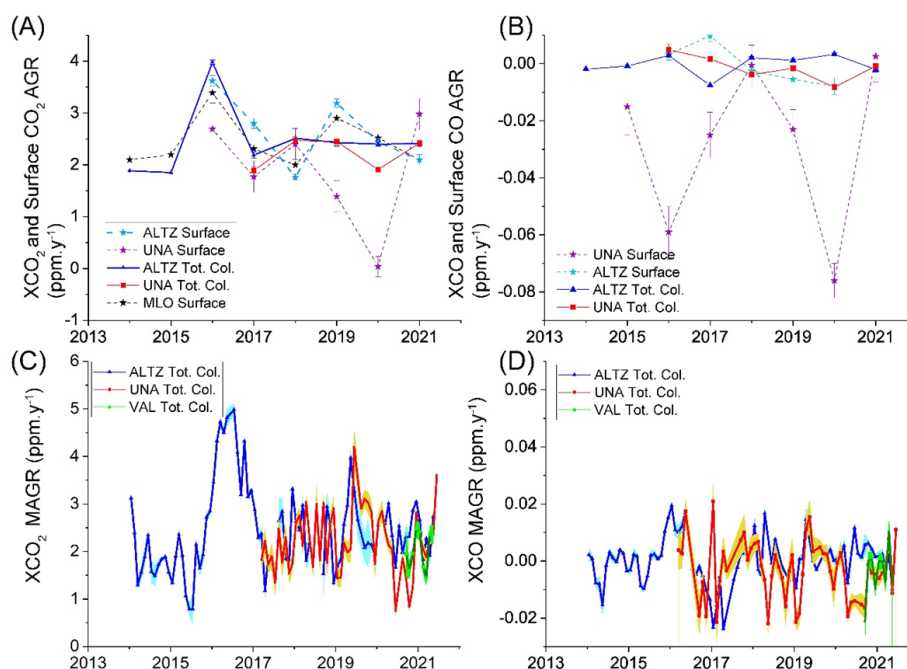
Figure 4: XCO_2 (A) and XCO (B) annual growth rates (AGR) and XCO_2 (C) and XCO (D) monthly-sampled annual growth rate (MAGR) obtained from total column and surface measurements for UNA, VAL, and ALTZ stations. In (A), the Mauna Loa (MLO) AGR trend was added in black dash-line. In (A) and (B) errors bars represent the standard error after removing annual cycles, reflecting the data sample quality. The standard error for the MAGR is shown as shaded area in (C) and (D).

449

450   Upon examining CO, the UNA XCO time series (Fig. 2C) has daily averages ranging between 0.10 and

451   0.23 ppm with a mean and standard deviation of 0.12 and 0.02 ppm, respectively, but shows a decreasing rate (-

452   4.0×10^{-3} ppm/year) over the whole measurement period. The VAL XCO time series show a very similar baseline

453   to UNA, with a daily average difference lower than 0.02 ppm for 85% of the coincident dataset (Fig. S1). At the

454   ALTZ background site, the XCO baseline and day-to-day variability are lower than at UNA and VAL, as expected

455   (mean and standard deviation equal to 0.08 and 0.01 ppm, respectively). The surface CO time series (Fig. 2D)

456   shows a more significant decreasing trend (-2.68×10^{-2} ppm/ year) than the total column data at UNA, while the

457   baseline at ALTZ remains constant around 0.11 ppm. The CO AGR and MAGR at ALTZ and UNA are shown in

458   Fig. 4B and D. Generally, the XCO AGR and MAGR oscillate around their base level at the ALTZ and UNA

459   stations, with short-term anomalies. At ALTZ, a strong negative XCO AGR anomaly is observed in 2017, which

460   was not observed for XCO_2, likely resulting from the exceptionally high XCO columns measured during 2016.

461   This is supported by the increase of the XCO MAGR from October 2015 to July 2016 (Fig. 4D), coinciding with

462   the first 10 months of the highest XCO_2 anomaly and followed by the lowest XCO MAGR values of the time series

463 (around -0.02 ppm/year in April 2017). At the UNA station, the AGR slightly decreases between 2016 and 2020

464 and increases again in 2021. The most significant and prolonged (>5 months) MAGR anomaly (Fig. 4D) occurred

465 between April and September 2020, with negative values. Some short-term additional anomalies are observed, but

466 only a few of them (in May 2018 and January 2019) are not affected by the limited number of available

467 measurements.

468 **4.2 Seasonal variability and short-term cyclic events**

469 Annual cycles are observed for both total column XCO_2 and CO_2 surface measurements at ALTZ, UNA and VAL

470 stations (Fig. 2). The minimum and maximum of the total column XCO_2 cycles are observed in May-June and

471 September, respectively, with an average amplitude around 5 (ALTZ) and 6 (UNA) ppm.

472 To examine the temporal changes in amplitude and shape of the annual cycles, total column data were monthly-

473 averaged, detrended by subtracting the linear part of the fit ($f(x) = ax$, in Eq. (7)), and compared to the detrended

474 mean annual cycle ($f(x) - ax$) in Fig. 3. To obtain a longer-term view, we included the 2013-2015 period from the

475 ALTZ station, previously published in Baylon et al. (2017), after applying the inter-calibration factors (section

476 3.1.3). At ALTZ, two periods significantly deviated from the average XCO_2 seasonal cycle, i.e.: (i) the year 2015,

477 where all the monthly averaged XCO_2 are below the fit and with one of the lowest seasonal amplitudes (~4.0 ppm)

478 of the whole time series, and (ii) the year 2016, with higher monthly averages than the mean XCO_2 seasonal cycle

479 and the highest amplitude (~5.8 ppm). At UNA, the difference with respect to the average XCO_2 seasonal cycle is

480 not significant, except for the year 2020, where all the monthly averages are below the mean annual cycle. During

481 this period, the UNA and VAL XCO_2 monthly-averaged data fit exceptionally well with those of the ALTZ station

482 between March 2020 and March 2021 in terms of shape and amplitude, while the UNA and VAL annual cycle

483 amplitudes are slightly higher than those of ALTZ for the other years.

484 Regarding the CO_2 surface data (Fig. 2B), annual cycles are observed with maxima and minima reached mid-

485 December and mid-September, respectively. As also reported in González del Castillo et al. (2022), the maximum

486 occurred during winter, when shallower boundary layer prevails and the summer-autumn minimum can be

487 explained by the dilution of trace gases in a deeper convective boundary layer and more active urban vegetation.

488 XCO peaks every year in April-May at the three stations (Fig. 2C and Fig. 3B) and then shows minimal annual

489 values in August, preceding by 1 month the minimum and maximum values of the XCO_2 time series. The April-

490 May maximal annual values, also confirmed by TROPOMI measurements (Borsdorff et al., 2020), coincide with

491 the biomass burning season and the periods during which the mixed layer reaches its maximum altitude (García-

492 Franco et al., 2018). During 2015, the XCO time series show a very low maximum reached in February instead of

493 May (Fig. 3B), contrasting with 2016, where high total column XCO values are reached in January and maintained

494 for a period of at least 5 months. Additionally, in 2018, the XCO annual cycles differ from the other years with

495 lower values and a flat shape during the first semester of the year (January-May).

496 Surface CO data (Fig. 2D) also show periodic increases at the ALTZ station with maxima reached during April-

497 May, coinciding with the maxima observed from total column XCO measurements. They confirm the increase of

498 the CO emissions during the biomass burning season, at least dominant in the ALTZ measurements. However, at

499 the UNA station, cycles are also observed in the surface data but with a maximum coinciding with that of the CO_2

500 surface data, and lagging behind the XCO total columns. These cycles are likely dominated by other processes

501 affecting both CO and CO_2 species such as the mixed layer seasonal dynamic.

502 **4.3 Intraday variability**

503   The intraday variability of the total columns and surface data are depicted in Fig. 5 and Fig. 6. Since the ALTZ

504   total column data do not present a significant diurnal pattern (the hourly variability remains lower than the standard

505   error of the time series), they are not presented in these plots.
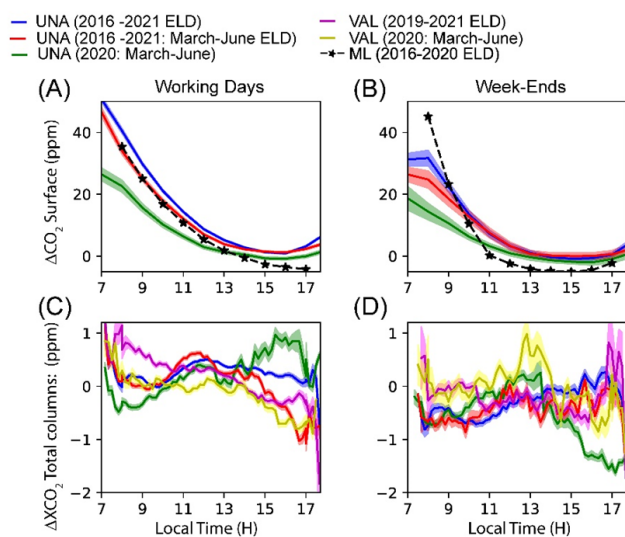

506

507   **Figure 5: Diurnal patterns of the detrended surface CO₂ mole fractions (A and B) and XCO₂ total columns (C and D)**
508   **measured at UNA and VAL stations. For each panel, the different curves represent different time periods: in blue, the**
509   **whole measurement period excluding the lock-down period (March-June 2020 ELD), in green the lock-down period**
510   **(March-June 2020) and in red the whole measurement periods from March to June, excluding the lock-down. The**
511   **standard errors are presented as shaded areas. Black curves represent the diurnal pattern of CO₂ in the Mixed Layer**
512   **(ML) calculated from the total columns data for the UNA station.**

513   Total column data were detrended by removing the seasonal fit (black traces in Fig. 2A and Fig. 2C), and averaged

514   over 10 min. To avoid a possible bias due to strong ventilation periods, a filter based on a ventilation index (VI)

515   was applied, following recommendations in Hardy (2001), Su et al. (2018) and Storey and Price (2022). The VI is

516   calculated as the product of average wind speed velocity (between the surface and 100 m height), and the planetary

517   boundary layer height for UNA and VAL locations. The wind velocity and the MLH were estimated with the U

518   and V wind components and the PBL height fields from the hourly ERA5 reanalysis product (Hersbach et al.,

519   2020). In the MCMA, the surface wind speed presents a diurnal pattern, generally reaching a maximum during the

520   afternoon between 14 and 15h LT (Fig. S4). The filter selects the days complying with the following criteria (i) a

521   maximum wind velocity (average 10-100m height) between 10h and 12h LT lower than 1.5 m.s^{-1} (threshold based

522   on Stremme et al., 2013) and (ii) a daily VI lower than 2350 m^2.s^{-1}, which represents a commonly used threshold

523   for selecting poor ventilation conditions (Hardy, 2001; Storey and Price, 2022). About 60% of the original XCO₂

524   and XCO dataset is selected by applying the filter, and will be considered in the following analysis. We note that

525   about 70% of discarded data corresponds to the January-May period of the year. Filtered total column XCO₂ and

526   XCO data were averaged by 10 min and presented in Fig. 5C-D and Fig. 6C-D, distinguishing between the working

527   days (WD) and the week-end (WE) periods. To explore the 2020 lock-down influence on the diurnal pattern, three

528   different periods were distinguished for each plot, the first one (blue trace) corresponding to the whole

529   measurement period excluding the interval in 2020 during which a significant MGRA decrease was observed

530 (March - October 2020 ELD) due to the lock-down period; the second (green trace: March- June 2020) only

531 includes the lock-down period, and additionally excludes the rainy season to avoid bias due to incomplete daily

532 time series; and the third period (red trace) is the same as the first one, but only considering the March to June

533 months to be compared with the lock-down period.
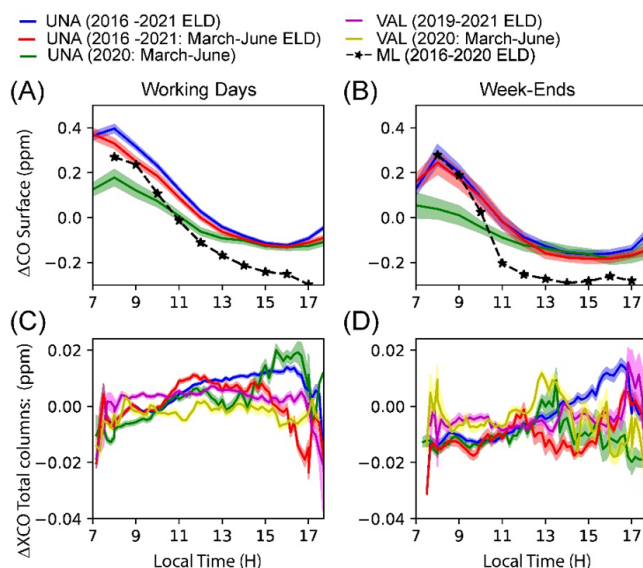
535 **Figure 6: Same as Figure 5, but from surface CO and total column XCO measurements.**

536 Surface data from the CRDS analyzers were detrended by removing the background fit following the methodology

537 described in the section 3.2, and filtered to be coincident with the filtered total column measurements (selection of

538 data between 7 and 18 h LT and only including the days with low ventilation conditions). They were finally

539 averaged by hours and presented in Fig. 5A-B and Fig. 6A-B for the WD and WE periods, respectively, for which

540 each curve represents the periods mentioned above.

541

542 The surface CO_2 diurnal pattern at UNA station for the whole measurement period (2016-2021, Fig. 5A and B in

543 blue) is consistent with the one previously described in Gonzalez del Castillo et al. (2022) for the 2014-2019

544 period, with a maximum observed during the early morning (reached before 7 h LT), a minimum during the

545 afternoon (between 15 and 16 h LT) and an average amplitude around 45 ppm. A lower amplitude of these cycles

546 is observed at WE (average amplitude of 28 ppm) with respect to the WD periods. During the 2020 lock-down

547 period (green curve), the WD surface CO_2 diurnal profile has a comparable amplitude (average amplitude of 26

548 ppm) to those of the WE for the whole measurement period, and slightly higher than that observed during the lock-

549 down WE periods (average amplitude of 22 ppm). The surface CO diurnal profile (Fig. 6: 2016-2021, blue curve)

550 peaks at 8h and then decreases until 16 h LT during any day of the week. The WD and WE data shows amplitudes

551 of up to 0.5 ppm and 0.3 ppm, respectively. During the lock-down period the WD and WE amplitudes are much

552 lower (0.3 and 0.2, respectively), consistently with the CO_2 surface observations.

553 The total columns XCO_2 and XCO diurnal patterns (Fig. 5C-D and Fig. 6C-D) have very different shapes than

554 those of the surface data, with amplitudes one order of magnitude lower. The variability observed between 7 and

555 8h is likely due to the low number of measurements during this time interval, and will not be taken into account in

556 the following analysis. The UNA and VAL XCO_2 diurnal patterns significantly differ in shape. The VAL WD

557 curve (magenta trace) continuously decreases from 8h to 17h (amplitude around 2 ppm) during both the whole

558 measurement and lock-down periods, but during the lockdown period, lower values are generally recorded with

559 higher intra-hour variability between 11h and 14h. The general WD decreasing trend suggests a maximum reached

560 during the early morning (before 7 h LT). This observation is supported by the CO_2 surface measurements

561 performed with the low-cost medium precision CO_2 sensors (Grutter et al., 2023), recording a maximum between

562 6h and 7h LT. The UNA XCO WD diurnal pattern (blue trace) is almost constant until 10h, then increases until

563 reaching a maximum around 12h, slightly decreases until 17h LT and finally shows an abrupt decrease after that.

564 The amplitude of the diurnal variability is around 1 ppm. During the lock-down period, the diurnal profile is

565 different, increasing until 12h LT, slightly decreasing until 13h LT and then increasing again until reaching a

566 maximum at 16h, and finally abruptly decreasing until 17h LT. The lock-down WD XCO_2 profile shows lower

567 values than the other periods until 13h, but the peak observed at 16h is not apparent for the other periods.

568 Variability is generally lower at WE (<1ppm), except for the lock-down period, for which an important decrease

569 is observed after 14h LT, but it is likely affected by a low number of measurement days. For XCO, the diurnal

570 profiles also have different shapes at UNA and VAL. At UNA, the March-June XCO diurnal profiles (red and

571 green curves) resemble that of XCO_2 for both the lock down and whole measurement periods. When considering

572 the twelve months of the year (blue trace), the maximum curve slightly increases between 12h and 16h, when it

573 reaches its maximum. It contrasts with the variability of the March to June months curves during this time interval,

574 for which an increase is observed during the lock-down period or a decrease if considering the whole measurement

575 period. At VAL, the diurnal profile is fairly constant until 17h with slightly lower values during the lock-down

576 period.

577 The total column XCO diurnal profiles at WE are less reliable with larger standard errors, likely due to the low

578 number of considered measurements. An increase is nevertheless observed at UNA where the considered day's

579 number is statistically more reliable, with a peak around 17h LT, which was not observed for XCO_2.

4.4 CO and CO_2 within the mixed layer from FTIR and surface data.

581 Figure 7 shows the hourly-averaged CO_2 and CO concentration within the mixed layer (CO_2^{ML} and CO^{ML}

582 products), calculated from the FTIR measurements (see section 3.4), concurrently to the surface data. The CO_2^{ML}

583 and CO^{ML} products are in agreement with the surface observation, with a slope of 0.95±0.02 (R^2=0.74) for CO_2

584 (Fig. 7C) and 0.81±0.02 (R^2=0.74) for XCO (Fig. 7D). For CO_2, the slope was found closer to 1.0 (1.00±0.02)

585 with an offset of -2.9±0.2 and a better R^2 (0.77) when discarding the data corresponding to the rainy season. This

586 effect is likely due to the removal of the incomplete daily time series frequently interrupted at the beginning of the

587 afternoon during the rainy season.

588
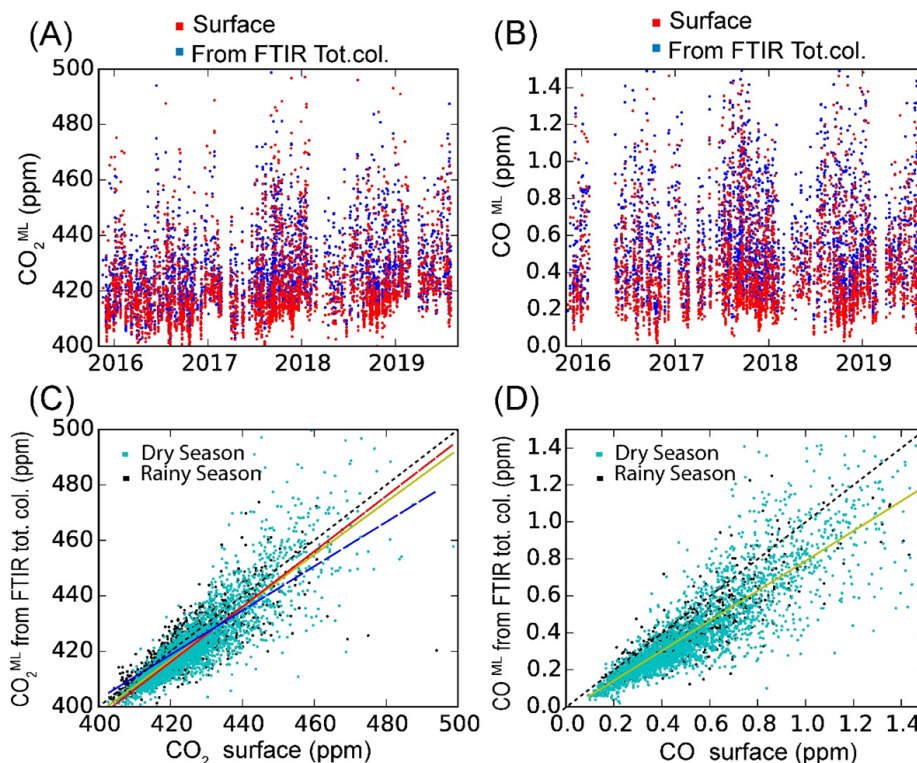
Figure 7: Comparison between (A) the CO_2^{ML} and (B) CO^{ML} products (red) derived from the ALTZ and UNA total column measurements and the surface measurements at the UNA station (blue). (C) and (D) represent the correlation plots for CO_2 and CO, respectively. In (C) and (D), we distinguished between data corresponding to the dry (November to May: cyan) and rainy (June to October: black) seasons. In (C), yellow, red and blue linear regression curves correspond to the whole measurement period (yellow: slope=0.95±0.02; Offset= 17.9±0.2; R^2=0.74), the dry season (red: slope=1.00±0.02; Offset: -2.9±0.2; R^2=0.77) and the rainy season (blue: slope=0.80±0.03; Offset: 83.7±0.39; R^2=0.66). In (D), since no significant difference was found for the different period, the regression line (yellow: slope=0.81±0.02; offset: -0.021±0.004; R^2=0.74) represent the whole measurement. The black dash line represents y=x.

The CO_2^{ML} and CO^{ML} diurnal patterns are presented in Fig. 5 and Fig. 6 (dash lines) together with those of surface measurements, after a similar filtering. The CO_2^{ML} and surface CO_2 diurnal patterns (Fig. 5A) are very similar in shape and amplitude, especially during the WD, although a small difference is observed at the end of the afternoon (<5 ppm). This difference is likely due to the increase of the uncertainties of the MLH estimate when it is more diluted. The CO^{ML} and surface CO diurnal profiles (Fig. 6A) also have similar amplitudes and shape for both WD and WE, although the CO^{ML} diurnal profile shows lower values (offset around 0.1 ppm at WD). Despite this very simplified model, these results show that the total column and surface measurements are mutually very consistent when the seasonal and diurnal variability of the ML expansion above Mexico City is taken into account.

4.5 XCO₂ to XCO enhancements ratios

607

608 The XCO and XCO_2 correlated enhancements and their ratio can give insights into the combustion efficiency of

609 the sources in a city, and therefore on their contributions. In this study we explored the variability of the

610 XCO/XCO_2 ratios at both long-term and intraday scales.

611 For the long-term analysis, the XCO_2 "background" level was calculated using a statistical method, using the lower

612 5th percentile of the measured Xgas over a 1-day running window (You et al., 2021). We did not use the ALTZ

613 measurements because of (i) the periodic influence of the wildfires in the region during the dry season, and (ii) the

614 discontinuity of our daily averaged time series. The enhancements above background $\Delta_m XCO_2$ and $\Delta_m XCO$

615 measured at UNA and averaged by months and their ratios are presented in Fig. 8, as whisker diagrams.
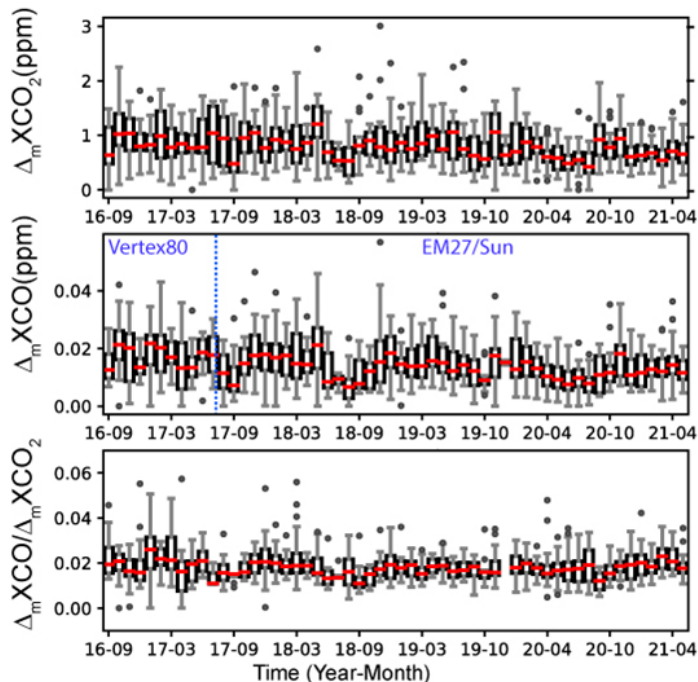
616

617 **Figure 8: Whisker diagram representing by month the variability of ΔXCO₂, ΔXCO and their ratio from the UNA**
618 **measurements.**

619 Both $\Delta_m XCO_2$ and $\Delta_m XCO$ time series show a slight decrease over time (around 0.05 ppm/year and 0.001

620 ppm/year, respectively). Although the $\Delta_m XCO/\Delta_m XCO_2$ ratio displays a variability around its mean value

621 (0.018±0.003), there are no discernible cyclic or long-term trend in the time series, except for the rainy periods of

622 2017, 2018 and 2020 when low ratios (and low $\Delta_m XCO$ and $\Delta_m XCO_2$ values) were observed. The $\Delta_m XCO$ and

623 $\Delta_m XCO/\Delta_m XCO_2$ ratio show a higher variability at the beginning of the time series (until July 2017) likely due to

624 the use of the CO Vertex products.

625

626 To perform the intraday analysis, the hourly-averaged data were first detrended by subtracting the daily average.

627 The resulting $\Delta_i XCO_2$ vs. $\Delta_i XCO$ datasets are plotted in Fig. 9A. The entire $\Delta_i XCO_2$ and $\Delta_i XCO$ datasets showed

628 a good correlation at both the UNA and VAL stations, with similar linear regression slopes around 0.0164±0.0003,

629   which is consistent with that found from the surface measurements and the ML product (Fig. 9B). Although there

630   is an actual difference in the emission types of the southern and northern parts of the city, the North hosting

631   industrial and commercial sources and the South being largely residential and commercial, the common and

632   dominant source of CO in the MCMA (at UNA and VAL stations) seems to incriminate motorised vehicles. The

633   data dispersion around the regression line likely reflects more punctual and local influence of other sources with

634   an important week-to-week variability.

635
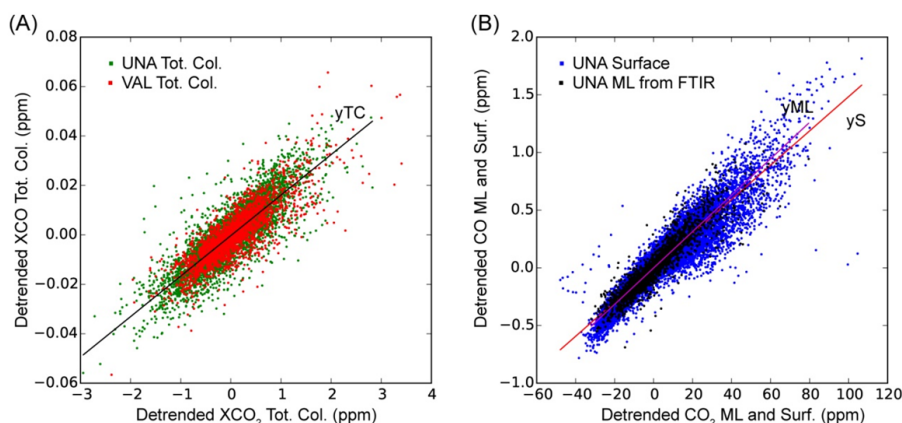
636
637
638 **Figure 9: A: Correlation plot of (A) the detrended (by removing the daily averages) hourly-average total column XCO_2**
639 **vs. XCO data, and (B) the detrended hourly average Mixing Layer (ML) and surface CO_2 vs. CO products. Solid lines**
640 **represent the linear regression lines, with the following parameters: TC slope=0.0164±0.0003, R^2=0.72 for the total**
641 **columns at UNA and VAL; yS slope=0.0148±0.0001, R^2=0.87 for the surface products and yML slope=0.0158±0.0002,**
642 **R^2=0.88 for the Mixing Layer products.**

643   On the other hand, the total column (UNA-VAL) differences, presented in Fig. S3 can also be used to calculate

644   the $\Delta XCO/\Delta XCO_2$ ratio, with a more precise subtraction of a common background (which assumes a

645   homogeneous background across the entire city) from the two stations. Figure 10 shows the hourly-average ΔXCO_2

646   (UNA-VAL) vs. ΔXCO (UNA-VAL) correlation plot for the coincident measurement period. A well-defined

647   linear correlation is observed with a slope of 0.015±0.001 and a coefficient of determination of R^2=0.80, highly

648   consistent with that found in Fig. 7. The use of the (UNA-VAL) total columns difference notably improved the

649   coefficient of determination, by removing the regional long-term and short-term perturbations affecting the two

650   sites. The intraday variability of the ΔXCO (UNA-VAL)/ΔXCO_2 (UNA-VAL) ratio (Fig. 10: colour scale),

651   showing higher columns at VAL during the morning and at UNA during the afternoon likely reflect the South to

652   North transport of air across the city. We note that the ratio remains the same during the lock-down period. We

653   would expect lower intraday (UNA-VAL) ΔXCO and ΔXCO_2 amplitudes during the lock-down period, but it is

654   not clearly apparent in this correlation plot.
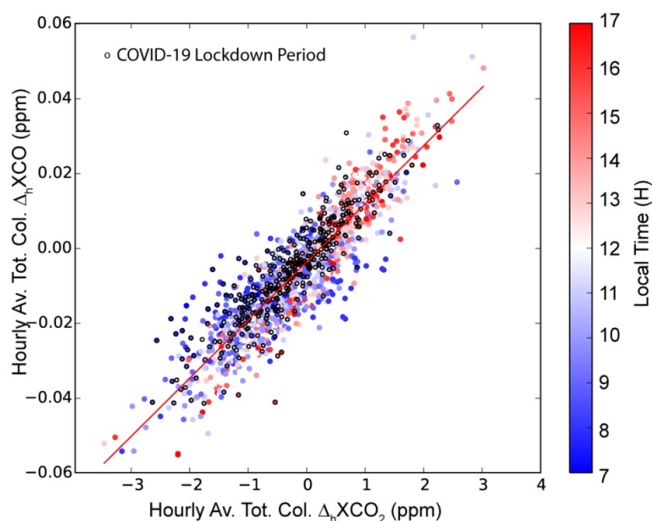
Figure 10: Correlation plot of the ΔXCO (UNA - VAL) vs. ΔXCO₂ (UNA - VAL) hourly averages (colour scale depending on the time is shown to the right) for the coincident measurement period (September 2019 - June 2021). Dots with black edges highlight the measurements during the COVID19 lock-down period (March-June 2020). Regression line (in red): Slope: 0.015±0.001, R²=0.80.

4.6 Estimate of CO and CO₂ MCMA emissions.

The variability of the long-term CO emissions in the MCMA can be estimated, following the method detailed in Stremme et al. (2013). In that study, they assumed that, since the XCO emissions in the MCMA are mainly due to traffic pollution, the rapid changes observed in the XCO total column (less affected by the airmass vertical distribution) should reflect the CO fresh emissions under certain meteorological conditions. Low ventilation, strong turbulence in the mixed layer and limited zenithal angle of measurements are critical criteria to avoid enhancement due to horizontal transport or local heterogeneity. XCO growth rates can be estimated at specific time intervals complying with these conditions from long-term time series. Further details on the method and estimates of uncertainties due to these assumptions are given in Stremme et al. (2013). Here, we determined an optimised time interval for estimating the mean CO growth rate using (i) the diurnal surface wind speed patterns and (ii) the MLH growth rate, the latter reflecting the turbulence within the mixed layer (Fig. S4). The time interval complying with a rapid growth of the mixed layer and low surface wind speed (< 2 m.s⁻¹) was found between 10 and 12h, which is in agreement with the requirements mentioned in Stremme et al. (2013). Growth rates and their uncertainties were determined by year, based on the linear regression (with 95% confidence interval) of the 10-min averaged detrended CO total columns over the 10-12h interval. For example, for the year 2018, we found a CO growth rate of 52 ± 5 kg.km^{-2}.h^{-1}.

To extrapolate the growth rate over the MCMA, we used the TROPOMI CO total column data that we averaged over the 2018-2022 period (Fig. 1), following the same method as described in Stremme et al. (2013). We assume that the total amount of fresh CO is proportional to the total emission of the MCMA and to the total column enhancement at the UNA site, which reflects the CO accumulated at this site. The ratio of the total accumulated CO in the MCMA to the accumulated CO at UNA is therefore the same as the emission ratio of the whole Megacity

681   to the emission flux at UNA. Therefore this ratio is the extrapolation factor and represents an effective area, defined

682   as Eq. (8):

683   $$Eff\_Area = \frac{\int (CO_{MCMA} - CO_{bgrd})}{CO_{UNA} - CO_{bgrd}} \qquad (8)$$

684   As the TROPOMI overflight time is around 13h30 LT, we cannot neglect the ventilation and slight advection is

685   smoothing out the distribution, so that both the background and the column at UNA have to be chosen carefully.

686   The background column was therefore estimated in two ways (i) from the smallest value observed upwind the city

687   at the elevation of the Mexican basin (contour line separating Mexico City from the Toluca area in the west in Fig.

688   1) and found to be 1.45×10^{18} molec.cm^{-2} and (ii) from the Tecamac site, where the border of MCMA was assumed

689   in the Stremme et al. (2013) and where the column was found to be 1.60×10^{18} molec.cm^{-2}.
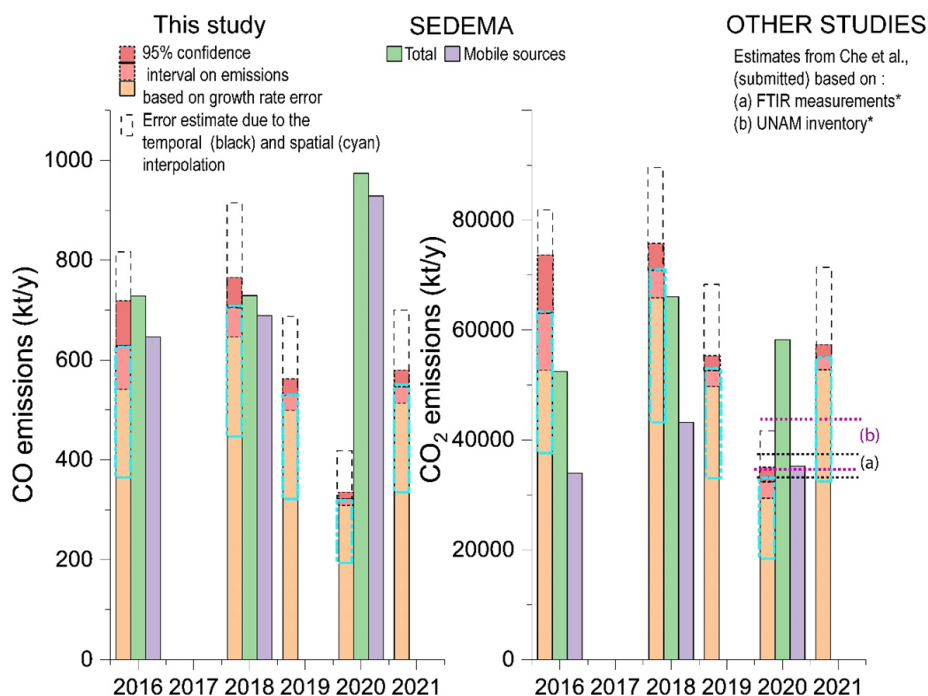
690   Due to advection, even locations slightly out of the megacity are presenting enhanced CO columns and it is not

691   clear which is the background column in the Mexican basin. Figure S5 illustrated the sensitivity of the effective

692   area to the background uncertainties. A 10% higher background leads to a 40% smaller extrapolation factor and a

693   40 % emission underestimate.

694   The mixed layer column at UNA from the TROPOMI data was found to be 1.93×10^{18} molec.cm^{-2} (Fig. 1), which

695   is consistent with our EM27/SUN ground-based measurements (average of 2.17×10^{18} molec.cm^{-2}). In cases where

696   the CO total column is lower than the background, likely due to the topography effect, we set the difference column

697   to zero for the integration. This topographic effect is important for the considered area, as there are plenty of

698   mountain around the basin, like the mountain ridge in the west (including Ajusco, Desierto de Leones, etc.), some

699   mountains in the mountain ridge on the eastern part of the area including in the south the two volcanoes

700   Popocatépetl and Iztaccihuatl. Finally, we found effective areas of ~2017 km^2 (outer area) and ~1178 km^2 (inner

701   area) considering the two background values given above. The "inner area" reflects conditions without ventilation

702   effect, therefore the outer area is more appropriate for the emission estimates given that the TROPOMI

703   measurements occurred at 13:30 when the ventilation cannot be neglected. The other estimates calculated from the

704   inner area will be thereafter only indicated within brackets and considered to estimate the sensitivity of the result.

705   Since the measured growth rate corresponds to a time interval of only 2 hours in the middle of the day, the CO

706   intraday fluctuations have to be taken into account. Stremme et al. (2013) used a factor which was taken from the

707   available bottom-up inventories and described that the CO emissions per/day are roughly 18.5 times the emission

708   per hour at noon. Assuming the same factor, we estimate a CO rate around 0.71±0.06 (0.42±0.04) Tg/year for

709   2018. If no information about the diurnal distribution of the emission rate would be available, we should assume

710   a uniform distribution and an upper value of the CO rate could be estimated using an intraday time interpolation

711   factor of 24 hours instead of 18.5, finally resulting in ~30% higher estimates. Despite the significant uncertainties

712   introduced by spatial and temporal interpolation, their impact on the relative variability, trends and anomalies of

713   the emission rates is less important if the same method and assumptions are consistently applied across the entire

714   time series.

715   CO_2 emissions could not be directly estimated using the same method, given its complex diurnal pattern, which is

716   a cumulative result of both natural and anthropogenic contributions and likely been influenced by additional

717   factors, related to instrumental and retrieval effects. Instead, we based our CO_2 estimates on the measured

718   XCO/XCO$_2$ ratio. The average XCO/XCO$_2$ molec. ratio (0.0164±0.0003) determined from the UNA and VAL

719 total column measurement (Fig. 9) was converted to a mass ratio (multiplying it by the molecular weight ratio)

720 and found to be 0.0100±0.0002. Considering this ratio, we estimated the CO_2 annual emission at 71±6 (42±4)

721 Tg/year for 2018. Our estimates of CO and CO_2 emissions by year and their average over the whole time series,

722 applying the same method, are presented in Fig. 11 and Table S3, concurrently with the SEDEMA inventories for

723 the MCMA. We obtained a 2016-2021 CO and CO_2 average emissions of 0.55±0.02 (0.32±0.01) and 46±2 (32±1)

724 Tg/year, respectively, when excluding the lockdown period (Table S3). Here, the given uncertainties are solely

725 those stemming from the propagation of errors in growth rate estimates. Uncertainties on absolute values are much

726 higher when considering spatial and temporal extrapolations errors, but they do not influence the interpretation of

727 relative values.

728

729 *Figure 11: Comparison of CO and CO_2 emission estimations from UNA FTIR diurnal growth rates and from SEDEMA*

730 *inventories. For CO_2 (right), the estimates from Che et al. (submitted) are also reported, although it was based on the 10/2020*

731 *to 05/2021 period, after applying the same intraday temporal factor as used for our study to convert the Gg/hour to t/year.*

732 **5 Discussion**

733 **5.1 Long term variability**

734 In this contribution, we characterised the seasonal and inter-annual variability and trends of the CO and CO_2 total

735 column and surface concentrations from two urban and one background stations. The average total column 2013-

736 2019 growth rate obtained at ALTZ (~2.5 ppm/year) and its inter-annual variability are in accordance with that

737 typical of the Northern Hemisphere measurements from TCCON stations (hereafter, NH-TCCON) (Sussman et

738 al., 2020: AGR of 2.4 ppm/year for the 2012-2019 period).

739 Both the NH-TCCON and ALTZ stations captured an important increase of the AGR in 2016 (+1.1 ppm/year for
740 the TCCON stations and +2.1 ppm/year for the ALTZ station with respect to 2015), coinciding with the most
741 intense ENSO (El Niño Southern Oscillation) event since the 1950s'. The impact of "El Niño" events on the carbon
742 cycle is not yet fully understood, although they are consistently accompanied by a global increase of XCO_2 due to
743 increasing drought in many regions and a decrease in global land carbon uptake. In 2016, an increase of 1.3
744 ppm/year was observed in the Mauna Loa in situ AGR with respect to 2015 (Betts et al., 2018), for which the
745 contribution of the 'El Niño' event was estimated at about 25%, the rest ascribed to an increase of the
746 anthropogenic emissions. In Mexico, the "El Niño" events are generally associated with a decrease in
747 precipitations, with deficits which can reach up to 250 mm in the South-Western area of the country, causing
748 drought and a higher occurrence of wild and forest fires (Bravo-Cabrera et al., 2018, González del Castillo et al.,
749 2020). Our observations from the ALTZ measurements highlight a much higher XCO_2 increase (+2.1 ppm/year)
750 during 2016 with respect to 2015 than that observed at the NH-TCCON stations. During this period a small increase
751 in the XCO MAGR ($\sim$ +0.02 ppm) is also observed at both ALTZ and UNA stations, maintaining the highest
752 values of the whole time series over more than 4 months. Assuming that the CO MAGR variability captured at the
753 ALTZ station during 2016 rather reflects a change in the global MCMA's emissions, we attempt to delineate the
754 global and local contributions in the 2016 XCO_2 ALTZ AGR increase. Adopting a molecular CO/CO_2 ratio of $\sim$
755 0.016, a hypothetical increase of the XCO_2 MAGR over the 09/2015 - 09/2016 period due to the local emissions
756 would be around +1.2 ppm/year, thus about 60% of the observed increasing rate during this period (+2.1 ppm/year).
757 This gross estimate suggests that the El Niño regional effect only contributed at about 25% (0.9 ppm) to the
758 observed GRA increase, which is close to the estimate from the NH-TCCON stations ($\sim$ +1.1 ppm) and from in
759 situ data.
760 On the other hand, our long-term FTIR and surface time series allows examining the effect of the COVID-19 lock-
761 down on the tropospheric CO_2 and CO concentration above the MCMA at local and regional scales. The reduction
762 of the surface CO and CO_2 AGR at UNA (CO_2 AGR to a value close to zero, and CO AGR $\sim$ -0.1 ppm/year) with
763 respect to the other years (Fig. 4), and the strong diminution of their amplitude in the mean diurnal cycles clearly
764 reflect a significant decrease of the local emissions near the UNA station, likely due to a drastic reduction of the
765 urban traffic (the average annual congestion level decreased from 52% in 2019 to 36% in 2020 in Mexico City,
766 from TomTom available estimates https://www.tomtom.com/traffic-index/mexico-city-traffic/).
767 The FTIR total column XCO_2 and XCO time series at UNA did not capture such a drastic change, only a small
768 punctual decrease of the MAGR lower than the standard deviation of the whole time series was observed between
769 April and October 2020. These results are in accordance with previous studies in other parts of the world. Although
770 a reduction of 8.8% of the global CO_2 emissions was observed during the first five months of 2020 (Liu et al.,
771 2020; Jones et al., 2020) and an annual reduction from 4 to 7% (Le Quéré et al., 2020), the atmospheric total
772 column XCO_2 showed a less clear effect (Sussman et al., 2020).

773 **5.2 CO/CO_2 ratio and MCMA emission estimates**

774 In this study, we robustly determined the CO/CO_2 ratio characterising the combustion efficiency of the city
775 (0.016±0.01) from both surface and total column measurements at two urban stations. We found the same ratio for
776 the UNA and VAL stations, and this ratio is very consistent with that found using the (UNA-VAL) gradients and
777 using the surface measurements. This ratio is also consistent with that reported by MacDonald et al. (2023),

778   calculated from TROPOMI and OCO-2/3 measurements (0.019) and slightly higher than that obtained from the

779   EDGAR, FFDAS and ODIAC inventories (ratio ~0.012) reported in the same study.

780   Our estimate of CO emissions from the UNA measurements is based on a simplified approach, limited to

781   days with low ventilation and time intervals corresponding to the late morning hours. It assumes a homogeneous

782   area in the footprint and averages selected days without discrimination. Given that the temporal and spatial

783   extrapolation introduces large uncertainties, only the relative and interannual behaviour of the emission can be

784   discussed here, but the approach demonstrates how close column growth rate can be related to emission flux, if

785   meteorological conditions allow neglecting advection. Our estimated range of CO emissions are consistent with

786   the SEDEMA inventories at least for the year 2016 (factor 0.98) and 2018 (factor 1.04) if considering that they are

787   dominated by the mobile sources. However, it is not the case for 2020, for which our estimate is much lower than

788   SEDEMA by a factor of 0.3. During the lock-down period we estimated a decrease of about 55% compared to

789   2018 while in the SEDEMA report, 2020 is the year with the maximum CO emissions (increase of 35% compared

790   to 2018 considering the mobile sources). Both of these estimates contrast with Kutralam-Muniasamy et al. (2021),

791   which reported an increase of 1.1% during the lock-down using the RAMA surface data. The large difference

792   observed between these different studies can be due to i) the different methods used for extrapolating in space and

793   time the emissions, ii) higher uncertainties of the FTIR-based estimates due to an important reduction the selected

794   days of measurements and iii) an over-estimation of the SEDEMA inventory due to a lack of data during the lock-

795   down period. Our estimate is based on the extrapolation of data from only one station (UNA), for which the

796   dominant source is mainly the UNAM traffic activity. During the lockdown, the UNAM was closed and a

797   significant reduction of the local traffic was recorded, but this traffic reduction was likely not representative of the

798   whole MCMA. However, the decrease of the MGRA at both VAL and UNA stations does not support the increase

799   of the CO emissions estimated by the SEDEMA inventory. Interestingly, it was not possible to apply the same

800   method to calculate CO emissions at VAL because the average growth rate was close to zero (Fig. 6). This

801   behaviour at VAL is likely due to the fast dispersion of the pollutant at this site, weakening the link between the

802   diurnal pattern and the emissions.

803   Regarding CO_2, our estimates also agree with the SEDEMA's inventory, especially if we consider the total

804   emissions instead of mobile sources (factor of 1.2 and 1.1) for the years 2016 and 2018. For 2020, we estimated a

805   decrease of 55% while the SEDEMA inventory indicates a decrease of about 10%. The SEDEMA CO/CO_2 ratios

806   for total emissions are similar to ours (0.014 and 0.011 in 2016 and 2018, respectively). This result suggests that

807   the CO/CO_2 ratio we determined does not exclusively reflect the traffic emissions, as expected, but should have

808   another component. The SEDEMA ratios are higher for mobile sources (0.019 and 0.016 in 2016 and 2018,

809   respectively) and one order of magnitude lower for industrial and domestic burning, which represent the second

810   main CO_2 anthropogenic sources. If we consider the 2018 SEDEMA ratio for mobile sources (0.016), we find CO_2

811   emissions of the order of 43,100 kt/year for this year, within ~5% of the SEDEMA estimates.

812   Our results were also compared with the estimates reported in Che et al. (submitted), based on an intensive FTIR

813   measurement campaign performed during the 10/2020 to 05/2021 period and using a Column-Stochastic Time-

814   Inverted Lagrangian Transport model (X-STILT) and a bayesian inversion (Fig. 11). Considering the same

815   measurement period, our method leads to CO_2 emission estimates ranging between 29,000 and 49,800 kt/year

816   using inner and outer effective area, respectively, which is consistent with the estimates obtained in Che et al.

817   (submitted), ranging between 32,700 and 37,200 kt/year when applying the same intraday temporal extrapolation

818 factor. Although the method we used for estimating the MCMA emissions is coarse and contains large
819 uncertainties, mainly due to the temporal and space extrapolation, it shows the ability to use one station capturing
820 the variability of the anthropogenic emissions of the MCMA and providing a year-by-year follow-up emission
821 information without using complex dispersion models.

822 **6 Summary and conclusion**

823 We have analysed the variability of the total column XCO and XCO_2 above the MCMA from two urban and one
824 background stations. The long-term XCO_2 data at the ALTZ station shows an average annual growth rate of ~2.5
825 ppm/year, similar to what has been reported from TCCON stations in the northern hemisphere, and captured the
826 perturbation driven by the 2015-2016 El Niño event. The urban stations show a similar growth rate (~2.3 ppm/year)
827 and unlike at ALTZ, a slight decrease of XCO_2 and XCO during the COVID19 lock-down period could be
828 observed. The CO_2 and CO concentrations within the mixed layer, estimated from the FTIR total column
829 measurements and ceilometer data, were found to be consistent with the surface measurements. These findings
830 confirm that the concentrations near the surface are mainly controlled by the emissions and the daily behaviour of
831 the mixed layer in MCMA. Our long-term total column and surface time series from both urban stations allowed
832 us to determine with great confidence an average CO/CO_2 ratio, indicative of the Mexico City combustion
833 efficiency. The CO/CO_2 ratio over our long-term measurement period seems to be fairly constant and equals ~
834 0.016 (mass ratio: 0.010). This value is consistent with other studies such as from satellite measurements (OCO-
835 2/3 and TROPOMI) and the bottom-up inventories reported by MacDonald et al. (2023). Finally, we estimated the
836 CO emissions using the average daily growth rate determined from measurements at the UNA station. Although
837 this method likely leads to an under-estimate of the emissions due to the non-negligible effects to the advection,
838 our results were found to be very consistent with the 2016 and 2018 SEDEMA inventories. The same strategy
839 could not be applied at the VAL station likely because of the dominant and rapid transport of the air masses before
840 noon, preventing them from accumulating. The UNA station is located near a topographic barrier (the
841 Chichinautzin mountain range), which favours regional turbulence and rapid homogenization of the air masses,
842 making the total column measurements representative of the emissions. We finally estimated the CO_2 emissions
843 using the CO growth rate and the CO/CO_2 ratio. The finding that our CO_2 emission estimates are within 20% of
844 those of SEDEMA for total emissions show that our ratio reflects not only the traffic sources but is also affected
845 by other sources such as industrial activities and domestic burning. The UNA station, with its advantageous
846 orography, is therefore a good site to capture well-mixed emissions from the city and serves as a site to follow the
847 interannual variability and trends of the emissions in this urban environment. Finally, this study showed the
848 feasibility to monitor the long-term evolution of anthropogenic CO_2 and CO emissions in Mexico City by
849 deploying only a few EM27/SUN instruments.

850 **7 Author contribution**

851 All the co-authors contributed in the discussion of concepts, and to the preparation of the manuscript. NT, WS and
852 MG were responsible of FTIR measurements and the data analysis. MG and WS lead the ALTZ station
853 development and its long-term operation. AB and EGC were responsible of the maintenance of the instruments at
854 the Altzomoni station. VA helped to classify the days and hours with low ventilation and strong turbulence and

855 provided the UNAM emission inventory. EGC was in charge of the in-situ measurements, with the support of OL.
856 MG and MR led the MERCI-CO2 project. FH lead at KIT the German-Mexican collaboration for the deployment
857 of the high resolution FTIR spectrometer and supports its long-term operation as part of NDACC. FH has helped
858 in the design and setup of the spectrometer and solar tracker before it was shipped to Mexico. He has developed
859 the retrieval code PROFFIT and gives continuously support to the UNAM group for its use and in operating the
860 spectrometer. FH and CA lead the German-Mexican collaboration and give precious help for the EM27/Sun
861 measurements in the frame of the COCCON network. All the co-authors contributed of the redaction of the
862 manuscript.

863 **8 Competing interests**

864 The authors declare that they have no conflict of interest.

865 **9 Acknowledgements**

875

876 **10 References**

877 Alberti Arroyo, C. A.: Ground based FTIR and MAX-DOAS observations of greenhouse and trace gas
878 emissions in the Rhine valley (Germany), St. Petersburg and Yekaterinburg (Russia), Karlsruher Institut für
879 Technologie (KIT), https://doi.org/10.5445/IR/1000162056/v2, 2023.
880 Alberti, C., Hase, F., Frey, M., Dubravica, D., Blumenstock, T., Dehn, A., Castracane, P., Surawicz, G., Harig,
881 R., Baier, B. C., Bès, C., Bi, J., Boesch, H., Butz, A., Cai, Z., Chen, J., Crowell, S. M., Deutscher, N. M., Ene, D.,
882 Franklin, J. E., García, O., Griffith, D., Grouiez, B., Grutter, M., Hamdouni, A., Houweling, S., Humpage, N.,
883 Jacobs, N., Jeong, S., Joly, L., Jones, N. B., Jouglet, D., Kivi, R., Kleinschek, R., Lopez, M., Medeiros, D. J.,
884 Morino, I., Mostafavipak, N., Müller, A., Ohyama, H., Palmer, P. I., Pathakoti, M., Pollard, D. F., Raffalski, U.,
885 Ramonet, M., Ramsay, R., Sha, M. K., Shiomi, K., Simpson, W., Stremme, W., Sun, Y., Tanimoto, H., Té, Y.,
886 Tsidu, G. M., Velazco, V. A., Vogel, F., Watanabe, M., Wei, C., Wunch, D., Yamasoe, M., Zhang, L., and Orphal,
887 J.: Improved calibration procedures for the EM27/SUN spectrometers of the COllaborative Carbon Column
888 Observing Network (COCCON), Atmospheric Measurement Techniques, 15, 2433–2463,
889 https://doi.org/10.5194/amt-15-2433-2022, 2022.
890 Babenhauserheide, A., Hase, F., and Morino, I.: The Fossil Fuel Emissions of Tokyo estimated directly from
891 measurements of the Tsukuba TCCON site, Gases/Remote Sensing/Data Processing and Information Retrieval,
892 https://doi.org/10.5194/amt-2018-224, 2018.
893 Baylon, J. L., Stremme, W., Grutter, M., Hase, F., and Blumenstock, T.: Background
894 CO_2 levels and error analysis from ground-based solar absorption IR measurements in
895 central Mexico, Atmos. Meas. Tech., 10, 2425–2434, https://doi.org/10.5194/amt-10-2425-2017, 2017.

896   Betts, R. A., Jones, C. D., Knight, Jeff. R., Keeling, Ralph. F., Kennedy, John. J., Wiltshire, A. J., Andrew, R.
897   M., and Aragão, L. E. O. C.: A successful prediction of the record CO_2 rise associated with the 2015/2016 El
898   Niño, Phil. Trans. R. Soc. B, 373, 20170301, https://doi.org/10.1098/rstb.2017.0301, 2018.
899   Bezanilla, A., Krüger, A., Stremme, W., and Grutter, M.: Solar absorption infrared spectroscopic
900   measurements over Mexico City: Methane enhancements, Atmósfera, 27, 173–183,
901   https://doi.org/10.1016/S0187-6236(14)71108-7, 2014.
902   Borsdorff, T., Hasekamp, O. P., Wassmann, A., and Landgraf, J.: Insights into Tikhonov regularization:
903   application to trace gas column retrieval and the efficient calculation of total column averaging kernels, Atmos.
904   Meas. Tech., 7, 523–535, https://doi.org/10.5194/amt-7-523-2014, 2014.
905   Borsdorff, T., Aan de Brugh, J., Hu, H., Aben, I., Hasekamp, O., and Landgraf, J.: Measuring Carbon
906   Monoxide With TROPOMI: First Results and a Comparison With ECMWF-IFS Analysis Data, Geophysical
907   Research Letters, 45, 2826–2832, https://doi.org/10.1002/2018GL077045, 2018.
908   Borsdorff, T., García Reynoso, A., Maldonado, G., Mar-Morales, B., Stremme, W., Grutter, M., and Landgraf,
909   J.: Monitoring CO emissions of the metropolis Mexico City using TROPOMI CO observations, Atmos. Chem.
910   Phys., 20, 15761–15774, https://doi.org/10.5194/acp-20-15761-2020, 2020.
911   Bravo Cabrera, J. L., Azpra Romero, E., Rodriguez Gonzalez, F. J., and Rodriguez López, O.: Effects of ENSO
912   on precipitation in Mexico City, Investigaciones Geográficas, https://doi.org/10.14350/rig.59679, 2018.
913   Buchwitz, M., Reuter, M., Schneising, O., Noël, S., Gier, B., Bovensmann, H., Burrows, J. P., Boesch, H.,
914   Anand, J., Parker, R. J., Somkuti, P., Detmers, R. G., Hasekamp, O. P., Aben, I., Butz, A., Kuze, A., Suto, H.,
915   Yoshida, Y., Crisp, D., and O'Dell, C.: Computation and analysis of atmospheric carbon dioxide annual mean
916   growth rates from satellite observations during 2003–2016, Atmos. Chem. Phys., 18, 17355–17370,
917   https://doi.org/10.5194/acp-18-17355-2018, 2018.
918   Burgos-Cuevas, A., Magaldi, A., Adams, D. K., Grutter, M., García Franco, J. L., and Ruiz-Angulo, A.:
919   Boundary Layer Height Characteristics in Mexico City from Two Remote Sensing Techniques, Boundary-Layer
920   Meteorol, 186, 287–304, https://doi.org/10.1007/s10546-022-00759-w, 2023.
921   Che, K., Cai, Z., Liu, Y., Wu, L., Yang, D., Chen, Y., Meng, X., Zhou, M., Wang, J., Yao, L., and Wang, P.:
922   Lagrangian inversion of anthropogenic CO_2 emissions from Beijing using differential column measurements,
923   Environ. Res. Lett., 17, 075001, https://doi.org/10.1088/1748-9326/ac7477, 2022.
924   Chen, J., Viatte, C., Hedelius, J. K., Jones, T., Franklin, J. E., Parker, H., Gottlieb, E. W., Wennberg, P. O.,
925   Dubey, M. K., and Wofsy, S. C.: Differential column measurements using compact solar-tracking spectrometers,
926   Atmos. Chem. Phys., 16, 8479–8498, https://doi.org/10.5194/acp-16-8479-2016, 2016.
927   Chevallier, F., Deutscher, N. M., Conway, T. J., Ciais, P., Ciattaglia, L., Dohe, S., Fröhlich, M., Gomez-Pelaez,
928   A. J., Griffith, D., Hase, F., Haszpra, L., Krummel, P., Kyrö, E., Labuschagne, C., Langenfelds, R., Machida, T.,
929   Maignan, F., Matsueda, H., Morino, I., Notholt, J., Ramonet, M., Sawa, Y., Schmidt, M., Sherlock, V., Steele, P.,
930   Strong, K., Sussmann, R., Wennberg, P., Wofsy, S., Worthy, D., Wunch, D., and Zimnoch, M.: Global CO_2 fluxes
931   inferred from surface air-sample measurements and from TCCON retrievals of the CO_2 total column: TWO CO_2
932   FLUX INVERSIONS, Geophys. Res. Lett., 38, n/a-n/a, https://doi.org/10.1029/2011GL049899, 2011.
933   Duren, R. M. and Miller, C. E.: Measuring the carbon emissions of megacities, Nature Clim Change, 2, 560–
934   562, https://doi.org/10.1038/nclimate1629, 2012.
935   Frey, M., Sha, M. K., Hase, F., Kiel, M., Blumenstock, T., Harig, R., Surawicz, G., Deutscher, N. M., Shiomi,
936   K., Franklin, J. E., Bösch, H., Chen, J., Grutter, M., Ohyama, H., Sun, Y., Butz, A., Mengistu Tsidu, G., Ene, D.,
937   Wunch, D., Cao, Z., Garcia, O., Ramonet, M., Vogel, F., and Orphal, J.: Building the COllaborative Carbon
938   Column Observing Network (COCCON): long-term stability and ensemble performance of the EM27/SUN
939   Fourier transform spectrometer, Atmos. Meas. Tech., 12, 1513–1530, https://doi.org/10.5194/amt-12-1513-2019,
940   2019.
941   Frey, M. M., Hase, F., Blumenstock, T., Dubravica, D., Groß, J., Göttsche, F., Handjaba, M., Amadhila, P.,
942   Mushi, R., Morino, I., Shiomi, K., Sha, M. K., De Mazière, M., and Pollard, D. F.: Long-term column-averaged
943   greenhouse gas observations using a COCCON spectrometer at the high-surface-albedo site in Gobabeb, Namibia,
944   Atmos. Meas. Tech., 14, 5887–5911, https://doi.org/10.5194/amt-14-5887-2021, 2021.
945   García-Franco, J. L., Stremme, W., Bezanilla, A., Ruiz-Angulo, A., and Grutter, M.: Variability of the Mixed-
946   Layer Height Over Mexico City, Boundary-Layer Meteorol, 167, 493–507, https://doi.org/10.1007/s10546-018-
947   0334-x, 2018.
948   Gisi, M.: Setup of precise camera based solar tracker systems and greenhouse gas measurements using a
949   modified portable spectrometer, https://doi.org/10.5445/IR/1000031248, 2012.
950   Gisi, M., Hase, F., Dohe, S., and Blumenstock, T.: Camtracker: a new camera controlled high precision solar
951   tracker system for FTIR-spectrometers, Atmos. Meas. Tech., 4, 47–54, https://doi.org/10.5194/amt-4-47-2011,
952   2011.
953   Gisi, M., Hase, F., Dohe, S., Blumenstock, T., Simon, A., and Keens, A.: XCO2 measurements with a tabletop
954   FTS using solar absorption spectroscopy, Atmos. Meas. Tech., 5, 2969–2980, https://doi.org/10.5194/amt-5-2969-
955   2012, 2012.

Goldberg, D. L., Lu, Z., Oda, T., Lamsal, L. N., Liu, F., Griffin, D., McLinden, C. A., Krotkov, N. A., Duncan, B. N., and Streets, D. G.: Exploiting OMI NO2 satellite observations to infer fossil-fuel CO2 emissions from U.S. megacities, Science of The Total Environment, 695, 133805, https://doi.org/10.1016/j.scitotenv.2019.133805, 2019.

González Del Castillo, E., Taquet, N., Bezanilla, A., Stremme, W., Ramonet, M., Laurent, O, Xu, Y., Delmotte, M., Grutter, M.: CO2 variability in the Mexico City region from in situ measurements at an urban and a background site, Atm., 35, 377–393, https://doi.org/10.20937/ATM.52956, 2022.

Grutter, M.: Multi-Gas analysis of ambient air using FTIR spectroscopy over Mexico City, Atmosfera, 16, 1–13, 2003.

Grutter, M., Rivera, O., Retama, A., Contreras, J., González, E., Porras, S., López, O., Arredondo, T., Díaz, A., Robles, M., Sánchez B., Azpra, E., Ladino, L. Technical Report #4 in "EVALUACIÓN DE DISPOSITIVOS BASADOS EN MICROSENSORES PARA EL MONITOREO CONTINUO DE LA CALIDAD DEL AIRE", ICAyCC-UNAM 2023.

Grutter, M., Flores, E., Basaldud, R., & Ruiz-Suárez, L. G. (2003). Open-path FTIR spectroscopic studies of the trace gases over Mexico City. *ATMOSPHERIC AND OCEANIC OPTICS C/C OF OPTIKA ATMOSFERY I OKEANA*, *16*(3), 232-236.

Gurney, K. R., Liang, J., O'Keeffe, D., Patarasuk, R., Hutchins, M., Huang, J., Rao, P., and Song, Y.: Comparison of Global Downscaled Versus Bottom-Up Fossil Fuel CO $_2$ Emissions at the Urban Scale in Four U.S. Urban Areas, JGR Atmospheres, 124, 2823–2840, https://doi.org/10.1029/2018JD028859, 2019.

Hakkarainen, J., Szeląg, M. E., Ialongo, I., Retscher, C., Oda, T., and Crisp, D.: Analyzing nitrogen oxides to carbon dioxide emission ratios from space: A case study of Matimba Power Station in South Africa, Atmospheric Environment: X, 10, 100110, https://doi.org/10.1016/j.aeaoa.2021.100110, 2021.

Hardy, C. C.: Smoke management guide for prescribed and wildland fire, National Wildlife Coordinating Group, 2001.

Hase, F., Hannigan, J. W., Coffey, M. T., Goldman, A., Höpfner, M., Jones, N. B., Rinsland, C. P., and Wood, S. W.: Intercomparison of retrieval codes used for the analysis of high-resolution, ground-based FTIR measurements, Journal of Quantitative Spectroscopy and Radiative Transfer, 87, 25–52, https://doi.org/10.1016/j.jqsrt.2003.12.008, 2004.

Hase, F., Frey, M., Blumenstock, T., Groß, J., Kiel, M., Kohlhepp, R., Mengistu Tsidu, G., Schäfer, K., Sha, M. K., and Orphal, J.: Application of portable FTIR spectrometers for detecting greenhouse gas emissions of the major city Berlin, Atmos. Meas. Tech., 8, 3059–3068, https://doi.org/10.5194/amt-8-3059-2015, 2015.

Hase, F., Frey, M., Kiel, M., Blumenstock, T., Harig, R., Keens, A., and Orphal, J.: Addition of a channel for XCO observations to a portable FTIR spectrometer for greenhouse gas measurements, Atmospheric Measurement Techniques, 9, 2303–2313, 2016.

Hedelius, J. K., Viatte, C., Wunch, D., Roehl, C. M., Toon, G. C., Chen, J., Jones, T., Wofsy, S. C., Franklin, J. E., Parker, H., Dubey, M. K., and Wennberg, P. O.: Assessment of errors and biases in retrievals of XCO2, XCH4, XCO, and XN2O from a 0.5 cm−1 resolution solar-viewing spectrometer, Atmos. Meas. Tech., 9, 3527–3546, https://doi.org/10.5194/amt-9-3527-2016, 2016.

Hedelius, J. K., Liu, J., Oda, T., Maksyutov, S., Roehl, C. M., Iraci, L. T., Podolske, J. R., Hillyard, P. W., Liang, J., Gurney, K. R., Wunch, D., and Wennberg, P. O.: Southern California megacity CO$_2$, CH$_4$, and CO flux estimates using ground- and space-based remote sensing and a Lagrangian model, Atmos. Chem. Phys., 18, 16271–16291, https://doi.org/10.5194/acp-18-16271-2018, 2018.

Herrera, B., Bezanilla, A., Blumenstock, T., Dammers, E., Hase, F., Clarisse, L., Magaldi, A., Rivera, C., Stremme, W., Strong, K., Viatte, C., Van Damme, M., and Grutter, M.: Measurement report: Evolution and distribution of NH$_3$ over Mexico City from ground-based and satellite infrared spectroscopic measurements, Atmos. Chem. Phys., 22, 14119–14132, https://doi.org/10.5194/acp-22-14119-2022, 2022.

Hersbach, H., Bell, B., Berrisford, P., Hirahara, S., Horányi, A., Muñoz-Sabater, J., Nicolas, J., Peubey, C., Radu, R., Schepers, D., Simmons, A., Soci, C., Abdalla, S., Abellan, X., Balsamo, G., Bechtold, P., Biavati, G., Bidlot, J., Bonavita, M., De Chiara, G., Dahlgren, P., Dee, D., Diamantakis, M., Dragani, R., Flemming, J., Forbes, R., Fuentes, M., Geer, A., Haimberger, L., Healy, S., Hogan, R. J., Hólm, E., Janisková, M., Keeley, S., Laloyaux, P., Lopez, P., Lupu, C., Radnoti, G., De Rosnay, P., Rozum, I., Vamborg, F., Villaume, S., and Thépaut, J.: The ERA5 global reanalysis, Quart J Royal Meteoro Soc, 146, 1999–2049, https://doi.org/10.1002/qj.3803, 2020.

Jones, C. D., Hickman, J. E., Rumbold, S. T., Walton, J., Lamboll, R. D., Skeie, R. B., Fiedler, S., Forster, P. M., Rogelj, J., Abe, M., Botzet, M., Calvin, K., Cassou, C., Cole, J. N. S., Davini, P., Deushi, M., Dix, M., Fyfe, J. C., Gillett, N. P., Ilyina, T., Kawamiya, M., Kelley, M., Kharin, S., Koshiro, T., Li, H., Mackallah, C., Müller, W. A., Nabat, P., Van Noije, T., Nolan, P., Ohgaito, R., Olivié, D., Oshima, N., Parodi, J., Reerink, T. J., Ren, L., Romanou, A., Séférian, R., Tang, Y., Timmreck, C., Tjiputra, J., Tourigny, E., Tsigaridis, K., Wang, H., Wu, M., Wyser, K., Yang, S., Yang, Y., and Ziehn, T.: The Climate Response to Emissions Reductions Due to COVID-19:

Initial Results From CovidMIP, Geophysical Research Letters, 48, e2020GL091883, https://doi.org/10.1029/2020GL091883, 2021.

Kiel, M., Eldering, A., Roten, D. D., Lin, J. C., Feng, S., Lei, R., Lauvaux, T., Oda, T., Roehl, C. M., Blavier, J.-F., and Iraci, L. T.: Urban-focused satellite CO2 observations from the Orbiting Carbon Observatory-3: A first look at the Los Angeles megacity, Remote Sensing of Environment, 258, 112314, https://doi.org/10.1016/j.rse.2021.112314, 2021.

Kutralam-Muniasamy, G., Pérez-Guevara, F., Roy, P. D., Elizalde-Martínez, I., and Shruti, V. C.: Impacts of the COVID-19 lockdown on air quality and its association with human mortality trends in megapolis Mexico City, Air Qual Atmos Health, 14, 553–562, https://doi.org/10.1007/s11869-020-00960-1, 2021.

Le Quéré, C., Jackson, R. B., Jones, M. W., Smith, A. J. P., Abernethy, S., Andrew, R. M., De-Gol, A. J., Willis, D. R., Shan, Y., Canadell, J. G., Friedlingstein, P., Creutzig, F., and Peters, G. P.: Temporary reduction in daily global CO2 emissions during the COVID-19 forced confinement, Nat. Clim. Chang., 10, 647–653, https://doi.org/10.1038/s41558-020-0797-x, 2020.

Lei, R., Feng, S., Danjou, A., Broquet, G., Wu, D., Lin, J. C., O'Dell, C. W., and Lauvaux, T.: Fossil fuel CO2 emissions over metropolitan areas from space: A multi-model analysis of OCO-2 data over Lahore, Pakistan, Remote Sensing of Environment, 264, 112625, https://doi.org/10.1016/j.rse.2021.112625, 2021.

Lian, J., Lauvaux, T., Utard, H., Bréon, F.-M., Broquet, G., Ramonet, M., Laurent, O., Albarus, I., Chariot, M., Kotthaus, S., Haeffelin, M., Sanchez, O., Perrussel, O., Denier Van Der Gon, H. A., Dellaert, S. N. C., and Ciais, P.: Can we use atmospheric CO $_2$ measurements to verify emission trends reported by cities? Lessons from a six-year atmospheric inversion over Paris, Gases/Atmospheric Modelling and Data Analysis/Troposphere/Physics (physical properties and processes), https://doi.org/10.5194/egusphere-2023-401, 2023.

Liu, Z., Ciais, P., Deng, Z., Lei, R., Davis, S. J., Feng, S., Zheng, B., Cui, D., Dou, X., Zhu, B., Guo, R., Ke, P., Sun, T., Lu, C., He, P., Wang, Y., Yue, X., Wang, Y., Lei, Y., Zhou, H., Cai, Z., Wu, Y., Guo, R., Han, T., Xue, J., Boucher, O., Boucher, E., Chevallier, F., Tanaka, K., Wei, Y., Zhong, H., Kang, C., Zhang, N., Chen, B., Xi, F., Liu, M., Bréon, F.-M., Lu, Y., Zhang, Q., Guan, D., Gong, P., Kammen, D. M., He, K., and Schellnhuber, H. J.: Near-real-time monitoring of global CO2 emissions reveals the effects of the COVID-19 pandemic, Nat Commun, 11, 5172, https://doi.org/10.1038/s41467-020-18922-7, 2020.

Lu, S., Wang, J., Wang, Y., and Yan, J.: Analysis on the variations of atmospheric CO $_2$ concentrations along the urban–rural gradients of Chinese cities based on the OCO-2 XCO $_2$ data, International Journal of Remote Sensing, 39, 4194–4213, https://doi.org/10.1080/01431161.2017.1415482, 2018.

MacDonald, C. G., Mastrogiacomo, J.-P., Laughner, J. L., Hedelius, J. K., Nassar, R., and Wunch, D.: Estimating enhancement ratios of nitrogen dioxide, carbon monoxide and carbon dioxide using satellite observations, Atmos. Chem. Phys., 23, 3493–3516, https://doi.org/10.5194/acp-23-3493-2023, 2023.

Makarova, M. V., Alberti, C., Ionov, D. V., Hase, F., Foka, S. C., Blumenstock, T., Warneke, T., Virolainen, Y. A., Kostsov, V. S., Frey, M., Poberovskii, A. V., Timofeyev, Y. M., Paramonova, N. N., Volkova, K. A., Zaitsev, N. A., Biryukov, E. Y., Osipov, S. I., Makarov, B. K., Polyakov, A. V., Ivakhov, V. M., Imhasin, H. Kh., and Mikhailov, E. F.: Emission Monitoring Mobile Experiment (EMME): an overview and first results of the St. Petersburg megacity campaign-2019, Gases/Remote Sensing/Instruments and Platforms, https://doi.org/10.5194/amt-2020-87, 2020.

Molina, L. T., Madronich, S., Gaffney, J. S., Apel, E., De Foy, B., Fast, J., Ferrare, R., Herndon, S., Jimenez, J. L., Lamb, B., Osornio-Vargas, A. R., Russell, P., Schauer, J. J., Stevens, P. S., Volkamer, R., and Zavala, M.: An overview of the MILAGRO 2006 Campaign: Mexico City emissions and their transport and transformation, Atmos. Chem. Phys., 10, 8697–8760, https://doi.org/10.5194/acp-10-8697-2010, 2010.

Park, H., Jeong, S., Park, H., Labzovskii, L. D., and Bowman, K. W.: An assessment of emission characteristics of Northern Hemisphere cities using spaceborne observations of CO2, CO, and NO2, Remote Sensing of Environment, 254, 112246, https://doi.org/10.1016/j.rse.2020.112246, 2021.

Plaza-Medina, E. F., Stremme, W., Bezanilla, A., Grutter, M., Schneider, M., Hase, F., and Blumenstock, T.: Ground-based remote sensing of O3 by high- and medium-resolution FTIR spectrometers over the Mexico City basin, Atmos. Meas. Tech., 10, 2703–2725, https://doi.org/10.5194/amt-10-2703-2017, 2017.

Rißmann, M., Chen, J., Osterman, G., Zhao, X., Dietrich, F., Makowski, M., Hase, F., and Kiel, M.: Comparison of OCO-2 target observations to MUCCnet – is it possible to capture urban XCO2 gradients from space?, Atmos. Meas. Tech., 15, 6605–6623, https://doi.org/10.5194/amt-15-6605-2022, 2022.

Rivera Cárdenas, C., Guarín, C., Stremme, W., Friedrich, M. M., Bezanilla, A., Rivera Ramos, D., Mendoza-Rodríguez, C. A., Grutter, M., Blumenstock, T., and Hase, F.: Formaldehyde total column densities over Mexico City: comparison between multi-axis differential optical absorption spectroscopy and solar-absorption Fourier transform infrared measurements, Atmos. Meas. Tech., 14, 595–613, https://doi.org/10.5194/amt-14-595-2021, 2021.

Rodgers, C. D.: Inverse Methods for Atmospheric Sounding: Theory and Practice, WORLD SCIENTIFIC, https://doi.org/10.1142/3171, 2000.

1074   Sha, M. K., De Mazière, M., Notholt, J., Blumenstock, T., Chen, H., Dehn, A., Griffith, D. W. T., Hase, F.,
1075   Heikkinen, P., Hermans, C., Hoffmann, A., Huebner, M., Jones, N., Kivi, R., Langerock, B., Petri, C., Scolas, F.,
1076   Tu, Q., and Weidmann, D.: Intercomparison of low- and high-resolution infrared spectrometers for ground-based
1077   solar remote sensing measurements of total column concentrations of CO2, CH4 and CO, Atmos. Meas. Tech.,
1078   13, 4791–4839, https://doi.org/10.5194/amt-13-4791-2020, 2020.
1079   Silva, S. J., Arellano, A. F., and Worden, H. M.: Toward anthropogenic combustion emission constraints from
1080   space-based analysis of urban CO_2 /CO sensitivity, Geophysical Research Letters, 40, 4971–4976,
1081   https://doi.org/10.1002/grl.50954, 2013.
1082   Storey, M. A. and Price, O. F.: Prediction of air quality in Sydney, Australia as a function of forest fire load
1083   and weather using Bayesian statistics, PLoS ONE, 17, e0272774, https://doi.org/10.1371/journal.pone.0272774,
1084   2022.
1085   Stremme, W., Ortega, I., and Grutter, M.: Using ground-based solar and lunar infrared spectroscopy to study
1086   the diurnal trend of carbon monoxide in the Mexico City boundary layer, Atmos. Chem. Phys., 9, 8061–8078,
1087   https://doi.org/10.5194/acp-9-8061-2009, 2009.
1088   Stremme, W., Grutter, M., Rivera, C., Bezanilla, A., Garcia, A. R., Ortega, I., George, M., Clerbaux, C.,
1089   Coheur, P.-F., Hurtmans, D., Hannigan, J. W., and Coffey, M. T.: Top-down estimation of carbon monoxide
1090   emissions from the Mexico Megacity based on FTIR measurements from ground and space, Atmos. Chem. Phys.,
1091   13, 1357–1376, https://doi.org/10.5194/acp-13-1357-2013, 2013.
1092   Su, T., Li, Z., and Kahn, R.: Relationships between the planetary boundary layer height and surface pollutants
1093   derived from lidar observations over China: regional pattern and influencing factors, Atmos. Chem. Phys., 18,
1094   15921–15935, https://doi.org/10.5194/acp-18-15921-2018, 2018.
1095   Sussmann, R. and Rettinger, M.: Can We Measure a COVID-19-Related Slowdown in Atmospheric CO2
1096   Growth? Sensitivity of Total Carbon Column Observations, Remote Sensing, 12, 2387,
1097   https://doi.org/10.3390/rs12152387, 2020.
1098   Toon, G., Blavier, J.-F., Washenfelder, R., Wunch, D., Keppel-Aleks, G., Wennberg, P., Connor, B., Sherlock,
1099   V., Griffith, D., Deutscher, N., and Notholt, J.: Total Column Carbon Observing Network (TCCON), in: Advances
1100   in Imaging, Advances in Imaging, Vancouver, journalAbbreviation: HISensE, JMA3, 2009.
1101   Viatte, C., Lauvaux, T., Hedelius, J. K., Parker, H., Chen, J., Jones, T., Franklin, J. E., Deng, A. J., Gaudet, B.,
1102   Verhulst, K., Duren, R., Wunch, D., Roehl, C., Dubey, M. K., Wofsy, S., and Wennberg, P. O.: Methane emissions
1103   from dairies in the Los Angeles Basin, Atmos. Chem. Phys., 17, 7509–7528, https://doi.org/10.5194/acp-17-7509-
1104   2017, 2017.
1105   Vogel, F. R., Frey, M., Staufer, J., Hase, F., Broquet, G., Xueref-Remy, I., Chevallier, F., Ciais, P., Sha, M. K.,
1106   Chelin, P., Jeseck, P., Janssen, C., Té, Y., Groß, J., Blumenstock, T., Tu, Q., and Orphal, J.:
1107 XCO_2 in an emission hot-spot region: the COCCON Paris campaign 2015, Atmos. Chem.
1108   Phys., 19, 3271–3285, https://doi.org/10.5194/acp-19-3271-2019, 2019.
1109   Wang, H., Jiang, F., Wang, J., Ju, W., and Chen, J. M.: Terrestrial ecosystem carbon flux estimated using
1110   GOSAT and OCO-2 XCO_2 retrievals, Atmos. Chem. Phys., 19, 12067–12082,
1111   https://doi.org/10.5194/acp-19-12067-2019, 2019.
1112   Wang, Y., Broquet, G., Bréon, F.-M., Lespinas, F., Buchwitz, M., Reuter, M., Meijer, Y., Loescher, A.,
1113   Janssens-Maenhout, G., Zheng, B., and Ciais, P.: PMIF v1.0: assessing the potential of satellite observations to
1114   constrain CO2; emissions from large cities and point sources over the globe using synthetic data, Geosci. Model
1115   Dev., 13, 5813–5831, https://doi.org/10.5194/gmd-13-5813-2020, 2020.
1116   Wu, D., Lin, J. C., Fasoli, B., Oda, T., Ye, X., Lauvaux, T., Yang, E. G., and Kort, E. A.: A Lagrangian
1117   approach towards extracting signals of urban CO2 emissions from satellite observations of atmospheric column
1118   CO2 (XCO2): X-Stochastic Time-Inverted Lagrangian Transport model ("X-STILT v1"), Geosci. Model Dev.,
1119   11, 4843–4871, https://doi.org/10.5194/gmd-11-4843-2018, 2018.
1120   Wunch, D., Wennberg, P. O., Toon, G. C., Keppel-Aleks, G., and Yavin, Y. G.: Emissions of greenhouse gases
1121   from a North American megacity, Geophysical Research Letters, 36, 2009GL039825,
1122   https://doi.org/10.1029/2009GL039825, 2009.
1123   Xu, Y., Lauvaux T., Grutter, M., Taquet, N., García-Reynoso, J.A., Laurent, O., Lopez, M., Lian, J., Lin, X.,
1124   Stremme, W., Ramonet, M., Atmospheric CO2 dynamics over a mountain urban basin: a case study of the Mexico
1125   City metropolitan area, submitted.
1126   Ye, X., Lauvaux, T., Kort, E. A., Oda, T., Feng, S., Lin, J. C., Yang, E., and Wu, D.: Constraining fossil fuel
1127 CO_2 emissions from urban area using OCO-2 observations of total column
1128 CO_2, Gases/Atmospheric Modelling/Troposphere/Physics (physical properties and
1129   processes), https://doi.org/10.5194/acp-2017-1022, 2017.
1130   You, Y., Byrne, B., Colebatch, O., Mittermeier, R. L., Vogel, F., and Strong, K.: Quantifying the Impact of the
1131   COVID-19 Pandemic Restrictions on CO, CO2, and CH4 in Downtown Toronto Using Open-Path Fourier
1132   Transform Spectroscopy, Atmosphere, 12, 848, https://doi.org/10.3390/atmos12070848, 2021.

1133   Zhang, Q., Boersma, K. F., Zhao, B., Eskes, H., Chen, C., Zheng, H., and Zhang, X.: Quantifying daily NO $_x$
1134   and CO $_2$ emissions from Wuhan using satellite observations from TROPOMI and OCO-2, Atmos. Chem. Phys.,
1135   23, 551–563, https://doi.org/10.5194/acp-23-551-2023, 2023.
1136   Zhao, X., Marshall, J., Hachinger, S., Gerbig, C., Frey, M., Hase, F., and Chen, J.: Analysis of total column
1137   CO2 and CH4 measurements in Berlin with WRF-GHG, Atmos. Chem. Phys., 19, 11279–11302,
1138   https://doi.org/10.5194/acp-19-11279-2019, 2019.
1139   Zhou, M., Ni, Q., Cai, Z., Langerock, B., Nan, W., Yang, Y., Che, K., Yang, D., Wang, T., Liu, Y., and Wang,
1140   P.: CO2 in Beijing and Xianghe Observed by Ground-Based FTIR Column Measurements and Validation to OCO-
1141   2/3 Satellite Observations, Remote Sensing, 14, 3769, https://doi.org/10.3390/rs14153769, 2022.